mathematics

MDPI

Article

Highly Accurate and Efficient Time Integration Methods with Unconditional Stability and Flexible Numerical Dissipation

Yi Ji [1,*] and Yufeng Xing [2,*]

[1] MOE Key Laboratory of Dynamics and Control of Flight Vehicle, School of Aerospace Engineering, Beijing Institute of Technology, Beijing 100081, China
[2] Institute of Solid Mechanics, Beihang University, Beijing 100083, China
* Correspondence: jiyi0319@outlook.com (Y.J.); xingyf@buaa.edu.cn (Y.X.)

Abstract: This paper constructs highly accurate and efficient time integration methods for the solution of transient problems. The motion equations of transient problems can be described by the first-order ordinary differential equations, in which the right-hand side is decomposed into two parts, a linear part and a nonlinear part. In the proposed methods of different orders, the responses of the linear part at the previous step are transferred by the generalized Padé approximations, and the nonlinear part's responses of the previous step are approximated by the Gauss–Legendre quadrature together with the explicit Runge–Kutta method, where the explicit Runge–Kutta method is used to calculate function values at quadrature points. For reducing computations and rounding errors, the 2^m algorithm and the method of storing an incremental matrix are employed in the calculation of the generalized Padé approximations. The proposed methods can achieve higher-order accuracy, unconditional stability, flexible dissipation, and zero-order overshoots. For linear transient problems, the accuracy of the proposed methods can reach 10^{-16} (computer precision), and they enjoy advantages both in accuracy and efficiency compared with some well-known explicit Runge–Kutta methods, linear multi-step methods, and composite methods in solving nonlinear problems.

Keywords: transient problems; generalized Padé approximations; Gauss–Legendre quadrature; high accuracy and efficiency

MSC: 37M05; 37M10; 70E55; 37M15

Citation: Ji, Y.; Xing, Y. Highly Accurate and Efficient Time Integration Methods with Unconditional Stability and Flexible Numerical Dissipation. *Mathematics* **2023**, *11*, 593. https://doi.org/10.3390/math11030593

Academic Editor: Sitnik Sergey

Received: 5 January 2023
Revised: 18 January 2023
Accepted: 20 January 2023
Published: 23 January 2023

1. Introduction

Owing to the complexity of practical problems, analytical solutions are generally not available for transient analyses, and thus numerical methods are pre-dominantly used to approximate the transient response. In finite element analyses (FEA) of transient problems, time integration methods [1] are widely used. A large number of time integration methods [1–3] have been developed over the last decades, and novel ones are continuously proposed. In commercial finite element software and also in scientific applications that are directed at studying transient problems, the Newmark method [1] and the HHT-α method [1] are popular.

In general, conventional time integration methods can be described as either implicit or explicit methods [1]. Explicit methods are conditionally stable in terms of the algorithm structure, causing an allowable time step size to be severely limited by stability in the simulations of dynamic systems. Implicit methods can achieve unconditional stability for linear systems, but considering that an iteration method is necessary for implicit methods, their computations are more expensive compared with explicit methods in the simulations of nonlinear systems.

For improving the accuracy of traditional single-step implicit methods, such as the Newmark [1], WBZ-α [1], and generalized-α methods [1], composite methods based on

the multi-sub-step concept are developed. The composite methods first appeared in the research of Bank and his co-workers [4], wherein they proposed a two-sub-step method consisting of the trapezoidal rule (TR) and the backward difference formula (BDF), and used it to analyze the transient behavior of silicon devices and circuits. Later, the two-sub-step based on TR and BDF was employed to solve structural dynamics by Bathe [5] in 2005, and the composite method was conceptualized. Motived by Bathe's work, composite methods that collect the advantage of the sub-step method attract wide attention and rapid development. The three-sub-step [6,7], four-sub-step [8,9], and five-sub-step [8,9] composite methods based on TR and BDF were constructed to obtain a higher low-frequency accuracy. Due to the use of BDF, the composite methods adopting the combinations of TR and BDF are L-stable (or asymptotically annihilating), meaning that the high-frequency modes are quickly eliminated. For flexibly controlling the amount of high-frequency numerical dissipation, composite methods including TR and backward interpolation formula (BIF) [10–13] have been proposed, such as the ρ_∞-Bathe method [10], the Kim method [11], and the TR-TR-BIF [12]. Among these methods, the TR-TR-BIF [12] proposed by the present authors has been generalized to the dynamic analysis of multibody systems [14] and structures under seismic response [15,16], further showing its superiority in the analysis of transient problems. Recently, composite methods with higher-order accuracy have been constructed [17–19], and they show a considerable advantage in phase accuracy compared with the second-order accurate composite methods.

Some time integration methods that are unconditionally stable for linear systems, such as the trapezoidal rule, may be unstable when applied to nonlinear systems [20,21], promoting the development of energy-conserving methods based on the energy constraint principle [22]. Therefore, different from most time integration methods, the equilibrium equations of motion at discrete time points cannot be satisfied for energy-conserving methods. The designs of most energy-conserving methods [23–25] are for nonlinear geometric systems, and energy-conserving methods can provide stable predictions for such types of transient problems. For dynamic systems, including nonlinear geometric and nonlinear damping terms, few energy-conserving methods, such as the ECM [26], have been constructed. The superiority of energy-conserving methods is that they can strictly keep energy for conservative systems, but they are not suitable for dynamic problems wherein some high-frequency information should be damped out. Additionally, the required modification of energy functions reduces the computational efficiency of this type of method.

To simultaneously improve the efficiency and stability of time integration methods, structure-dependent (or model-based) methods [27–32] were developed. In 2002, Chang proposed an unconditionally stable single-step method (noted as Chang2002) [27] for pseudo-dynamic systems, in which algorithmic parameters closely depend on dynamics characteristics at the initial moment and the selected size of the time step. The Chang2002 method achieves unconditional stability for linearity and stiffness softening systems. Based on the Chang2002 method, some more desirable structure-dependent methods [28–32] were constructed, such as the CR [28], KR [29], and Fu–Zhang methods [32]. Taking into account the properties of the model and the evolution of the computed fields, the locally adaptive time integration methods [33,34] proposed by Soares can reduce the contradiction of accuracy and efficiency. At present, this type of method has been applied in the analysis of wave propagation [35] and thermo-mechanical systems [36].

The emergence of exponential methods by making use of matrix theory reduces the contradiction of time integration methods in accuracy, efficiency, and stability. The so-called precise time integration method (PIM) for linear ordinarily differential equations (ODEs) proposed by Zhong and Williams [37] is a representative work wherein the Taylor series expansion is utilized to obtain the homogeneous solution, and the external excitations are assumed to be piecewise linear, and their contributions are obtained with the convolution integral. Due to the algorithmic structure, the PIM can converge to computer precision for homogeneous equations, and it is conditionally stable. Following the research of Zhong and Williams [37], some improved precise time integrators [38–42] were developed in

the past decades, such as the PEC/DMn [41] and the Song method [42]. The PEC/DMn proposed by the present authors possesses the advantages of the PIM in accuracy and efficiency, and it can achieve unconditional stability and exactly controllable dissipation. In addition to using existing time integration methods to approximate the amplification matrix, Song et al. [42] constructed higher-order precise integrators for linear wave propagation problems, in which the responses of the previous time step are transferred by the classical Padé expansion with L-stability, and the external force vectors are calculated based on a least-squares fit of the polynomial functions. An important feature of the higher scheme [42] is that no direct inversion of the mass matrix is required, further reducing its computational costs. At present, some exponential integrators [43–46] for nonlinear initial value problems have been constructed. In the type of methods, the responses of nonlinear terms at the present moment are replaced by the ones of the previous moment [45] or are approximated by the Euler method [43,44,46]. In comparison with traditional methods based on dynamics equilibrium equations, numerical experiments validate that exponential integrators [43–46] show improvements both in accuracy and efficiency in solving nonlinear transient problems.

From the above review, one can find that, in the past decades, various time integration methods have been developed for quickly, accurately, and/or stably solving transient problems. Among these methods, the exponential methods seem to be a superior candidate to fill the gap that stability, accuracy, and efficiency are hard to be simultaneously enhanced. Some exponential methods that are suitable both for linear and nonlinear problems have been applied in the analysis of elastodynamics [44], multibody dynamics [45], and so on, but these methods do not have the order of magnitude improvements in accuracy and/or efficiency compared with those of representative methods, such as the Newmark method and the Runge–Kutta method. In this context, focusing on the first-order linear and nonlinear initial value problems [47], this paper develops a new solution strategy. The combination of the generalized Padé expansion with A-stability [48], the 2^m algorithm, and the technology of storing incremental matrices is used in the calculation of responses of linear parts. The responses of nonlinear parts are approximated by the combination of the Gauss–Legendre quadrature formula and the explicit Runge–Kutta method. The two combinations can ensure that the proposed methods can accurately and quickly compute the responses of transient problems. Numerical experiments validate that when the proposed methods have the same computation as other methods, the accuracy of the proposed methods is greater than or equal to three orders of magnitude. The theoretical analysis finds that the time integration methods can obtain higher-order accuracy, unconditional stability, controllable dissipation, and zero-order overshoots. Therefore, the proposed methods are suitable both for conservative and non-conservative systems due to flexibly controllable numerical properties.

The rest of this work is organized as follows. The procedure of the new strategy is presented in Section 2. The numerical properties of the present methods, including stability, dissipation, accuracy, and overshoot characteristics, are analyzed in Section 3. Numerical experiments are implemented in Section 4. Finally, the conclusions are drawn in Section 5.

2. Basic Idea of the New Strategy

This paper focuses on the physically stable dynamic problems governed by the following first-order ordinary differential equation:

$$\dot{\boldsymbol{y}}(t) = \boldsymbol{H}\boldsymbol{y}(t) + \boldsymbol{f}(\boldsymbol{y}, t), \boldsymbol{y}(t_0) = \boldsymbol{y}_0, \tag{1}$$

where $\boldsymbol{H}$ is a matrix that includes eigenvalues with large negative real parts or with purely imaginary eigenvalues of large modulus [47], and the nonlinear term $\boldsymbol{f}$ is supposed to be a non-stiff satisfying the Lipschitz condition. If the term $\boldsymbol{f}$ only relates to time t, the nonlinear Equation (1) reduces to the linear one. The discretized dynamic system (1) arises in many applications [37–47,49–51], such as structural dynamics [39–41], multibody dynamics [45],

molecular dynamics [49], and so on. It is well-known that the general solution [47] of Equation (1) has the form of

$$\boldsymbol{y}_{t+\Delta t} = \mathrm{e}^{\Delta t \boldsymbol{H}} \boldsymbol{y}_t + \int_t^{t+\Delta t} \mathrm{e}^{\Delta t \boldsymbol{H}} \boldsymbol{f}(\boldsymbol{y}, \tau) \mathrm{d}\tau := \boldsymbol{A}_{\mathrm{ana}} \boldsymbol{y}_t + \boldsymbol{L}_{\mathrm{ana}}, \tag{2}$$

where the analytical amplification matrix $\boldsymbol{A}_{\mathrm{ana}} = \mathrm{e}^{\Delta t \boldsymbol{H}}$ can transfer the free responses of the previous step, and the forced responses of the current step are computed by the analytical vector $\boldsymbol{L}_{\mathrm{ana}} = \int_t^{t+\Delta t} e^{\Delta t \boldsymbol{H}} \boldsymbol{f}(\boldsymbol{y}, \tau) d\tau$. For practical systems, especially for large-scale problems, the computations of the matrix $\boldsymbol{A}_{\mathrm{ana}}$ and the vector $\boldsymbol{L}_{\mathrm{ana}}$ are expensive. The task of this strategy is to quickly construct highly accurate substitutes for $\boldsymbol{A}_{\mathrm{ana}}$ and $\boldsymbol{L}_{\mathrm{ana}}$.

In our work, the generalized Padé approximation [48] that is regarded as the most accurate rational approximation of $\exp(\Delta t \boldsymbol{H})$ is used to approximate $\boldsymbol{A}_{\mathrm{ana}}$, and the corresponding numerical matrix $\boldsymbol{A}_{\mathrm{num}}$ can be formulated as

$$\boldsymbol{A}_{\mathrm{num}}(\Delta t \boldsymbol{H}) = \bar{\boldsymbol{Q}}^{-1}(\Delta t \boldsymbol{H}) \bar{\boldsymbol{P}}(\Delta t \boldsymbol{H}), \tag{3}$$

where

$$\bar{\boldsymbol{Q}}(\Delta t \boldsymbol{H}) = (1-\rho_\infty)\boldsymbol{Q}_{n-1,n}(\Delta t \boldsymbol{H}) + 2\rho_\infty \boldsymbol{Q}_{n,n}(\Delta t \boldsymbol{H}), \bar{\boldsymbol{P}}(\Delta t \boldsymbol{H}) = (1-\rho_\infty)\boldsymbol{P}_{n-1,n}(\Delta t \boldsymbol{H}) + 2\rho_\infty \boldsymbol{P}_{n,n}(\Delta t \boldsymbol{H}), \text{ and} \tag{4}$$

$$\boldsymbol{P}_{i,j}(\Delta t \boldsymbol{H}) = \sum_{p=0}^{i} \frac{i!(j+i-p)!}{(i-p)!(j+i)!p!} (\Delta t \boldsymbol{H})^p, \boldsymbol{Q}_{i,j}(\Delta t \boldsymbol{H}) = \sum_{p=0}^{j} (-1)^p \frac{j!(j+i-p)!}{(j-p)!(j+i)!p!} (\Delta t \boldsymbol{H})^p, (i,j = 0,1,2,\ldots). \tag{5}$$

From Equations (3)–(5), one can observe that the generalized Padé approximations are the rational functions with polynomials of degree n in both the numerator and denominator. The generalized Padé approximation has A-stability; in addition, for the case of $0 \le \rho_\infty < 1$, it has $(2n-1)$th-order accuracy and $(2n)$th-order accuracy if $\rho_\infty = 1$. To further improve the accuracy of $\boldsymbol{A}_{\mathrm{num}}(\Delta t \boldsymbol{H})$ given in Equation (3), the 2^m algorithm and storage of incremental matrix technology are used in the preparation of $\boldsymbol{A}_{\mathrm{num}}(\Delta t \boldsymbol{H})$, which is shown below. Applying Equation (5) to Equation (3) can yield

$$\bar{\boldsymbol{Q}}(\Delta t \boldsymbol{H}) = \alpha_0 \boldsymbol{I} + \boldsymbol{S}_1(\Delta t \boldsymbol{H}), \bar{\boldsymbol{P}}(\Delta t \boldsymbol{H}) = \beta_0 \boldsymbol{I} + \boldsymbol{S}_2(\Delta t \boldsymbol{H}), \text{ and} \tag{6}$$

$$\boldsymbol{S}_1(\Delta t \boldsymbol{H}) = \alpha_1(\Delta t \boldsymbol{H}) + \alpha_2(\Delta t \boldsymbol{H})^2 + \cdots + \alpha_n(\Delta t \boldsymbol{H})^n, \boldsymbol{S}_2(\Delta t \boldsymbol{H}) = \beta_1(\Delta t \boldsymbol{H}) + \beta_2(\Delta t \boldsymbol{H})^2 + \cdots + \beta_n(\Delta t \boldsymbol{H})^n. \tag{7}$$

Then, the matrix $\boldsymbol{A}_{\mathrm{num}}(\Delta t \boldsymbol{H}) = \bar{\boldsymbol{Q}}(\Delta t \boldsymbol{H})^{-1} \bar{\boldsymbol{P}}(\Delta t \boldsymbol{H})$ that is equivalent to $\bar{\boldsymbol{Q}}(\Delta t \boldsymbol{H}) \boldsymbol{A}_{\mathrm{num}}(\Delta t \boldsymbol{H}) = \bar{\boldsymbol{P}}(\Delta t \boldsymbol{H})$ can be reformulated as

$$\begin{aligned} \left[\boldsymbol{I} + \tfrac{1}{\alpha_0}\boldsymbol{S}_1(\Delta t \boldsymbol{H})\right] \boldsymbol{A}_{\mathrm{num}}(\Delta t \boldsymbol{H}) &= \tfrac{\beta_0}{\alpha_0}\left[\boldsymbol{I} + \tfrac{1}{\alpha_0}\boldsymbol{S}_1(\Delta t \boldsymbol{H}) + \tfrac{1}{\beta_0}\boldsymbol{S}_2(\Delta t \boldsymbol{H}) - \tfrac{1}{\alpha_0}\boldsymbol{S}_1(\Delta t \boldsymbol{H})\right] \rightarrow \\ \boldsymbol{A}_{\mathrm{num}}(\Delta t \boldsymbol{H}) &= \tfrac{\beta_0}{\alpha_0}\left[\boldsymbol{I} + \left(\boldsymbol{I} + \tfrac{1}{\alpha_0}\boldsymbol{S}_1(\Delta t \boldsymbol{H})\right)^{-1}\left(\tfrac{1}{\beta_0}\boldsymbol{S}_2(\Delta t \boldsymbol{H}) - \tfrac{1}{\alpha_0}\boldsymbol{S}_1(\Delta t \boldsymbol{H})\right)\right] \\ &= \tfrac{\beta_0}{\alpha_0}\left[\boldsymbol{I} + \left(\boldsymbol{I} + \alpha_0 \boldsymbol{S}_1(\Delta t \boldsymbol{H})^{-1}\right)^{-1} \boldsymbol{S}_1(\Delta t \boldsymbol{H})^{-1}\left(\tfrac{\alpha_0}{\beta_0}\boldsymbol{S}_2(\Delta t \boldsymbol{H}) - \boldsymbol{S}_1(\Delta t \boldsymbol{H})\right)\right] \end{aligned}, \tag{8}$$

where the incremental matrix relative to the identity matrix $\boldsymbol{I}$ is defined as $\Delta \boldsymbol{S}(\Delta t \boldsymbol{H})$, as follows:

$$\Delta \boldsymbol{S}(\Delta t \boldsymbol{H}) = \left[\boldsymbol{I} + \alpha_0 \boldsymbol{S}_1(\Delta t \boldsymbol{H})^{-1}\right]^{-1} \boldsymbol{S}_1(\Delta t \boldsymbol{H})^{-1}\left[\frac{\alpha_0}{\beta_0}\boldsymbol{S}_2(\Delta t \boldsymbol{H}) - \boldsymbol{S}_1(\Delta t \boldsymbol{H})\right]. \tag{9}$$

The multi-sub-step notion is used to obtain a more accurate $\boldsymbol{A}_{\text{num}}(\Delta t\boldsymbol{H})$. Here, a time step size Δt is divided into $N = 2^m$ parts, leading to

$$\boldsymbol{A}_{\text{num}}(\Delta t\boldsymbol{H}) = \underbrace{\boldsymbol{A}_{\text{num}}(\Delta t_N\boldsymbol{H}) \quad \cdots \quad \boldsymbol{A}_{\text{num}}(\Delta t_N\boldsymbol{H})}_{N} = \boldsymbol{A}^N_{\text{num}}(\Delta t_N\boldsymbol{H}). \tag{10}$$

With the increase of m, the incremental matrix $\Delta\boldsymbol{S}(\Delta t_N\boldsymbol{H})$ is very small compared with the identity matrix $\boldsymbol{I}$, so during the calculation of Equation (10), the $\Delta\boldsymbol{S}(\Delta t_N\boldsymbol{H})$ is stored instead of $\boldsymbol{A}_{\text{num}}(\Delta t_N\boldsymbol{H})$ to reduce rounding errors. It is well-known that

$$(\boldsymbol{I} + \Delta\boldsymbol{S}(\Delta t_N)) \times (\boldsymbol{I} + \Delta\boldsymbol{S}(\Delta t_N)) = \boldsymbol{I} + 2\Delta\boldsymbol{S}(\Delta t_N) + \Delta\boldsymbol{S}(\Delta t_N) \times \Delta\boldsymbol{S}(\Delta t_N). \tag{11}$$

For calculating the matrix $\boldsymbol{A}_{\text{num}}(\Delta t\boldsymbol{H})$, Equation (11) should be iterated m times. Then, the calculation in Equation (10) is equivalent to executing the following statement

$$\begin{array}{c} \text{for } i = 1:1:m \\ \Delta\boldsymbol{S}(\Delta t_N) = 2\Delta\boldsymbol{S}(\Delta t_N) + \Delta\boldsymbol{S}(\Delta t_N) \times \Delta\boldsymbol{S}(\Delta t_N) \\ \text{end} \\ \boldsymbol{A}_{\text{num}}(\Delta t\boldsymbol{H}) = \left(\frac{\beta_0}{\alpha_0}\right)^{2^m}(\boldsymbol{I} + \Delta\boldsymbol{S}(\Delta t_N)) \end{array}. \tag{12}$$

After m times multiplication, the matrix $\Delta\boldsymbol{S}(\Delta t_N\boldsymbol{H})$ is no longer a very small matrix, and the above addition will have no serious numerical round-off error again. To show the accuracy advantage of the method of storing incremental matrix, a simple model is considered here, in which $\boldsymbol{H} = 1$ and $\Delta t = 0.1$. Table 1 provides absolute errors of the method of storing the total matrix and the method of storing the incremental matrix, and one can see that with the increase of m, (a) the former's accuracy firstly increases and then continuously decreases; (b) the errors of the latter trend to zero.

Table 1. Absolute errors of the method of storing total matrix and the method of storing incremental matrix.

	$m = 1$	$m = 10$	$m = 100$	$m = 1000$
Total	0.00267091807564768	$5.39597800242042 \times 10^{-6}$	0.105170918075648	0.105170918075648
increment	0.00267091807564768	$5.39597790183422 \times 10^{-6}$	0	0

Considering that the multi-sub-step notion is employed in the calculation of $\boldsymbol{A}_{\text{num}}(\Delta t\boldsymbol{H})$ for exactly controlling the amount of numerical dissipation via ρ_∞, the matrix $\boldsymbol{A}_{\text{num}}(\Delta t\boldsymbol{H})$ shown in Equation (3) for the case of $N \geq 1$ is reformulated as

$$\boldsymbol{A}_{\text{num}}(\Delta t\boldsymbol{H}) = \left[(1 - \sqrt[N]{\rho_\infty})\boldsymbol{Q}_{n-1,n}(\Delta t\boldsymbol{H}) + 2\sqrt[N]{\rho_\infty}\boldsymbol{Q}_{n,n}(\Delta t\boldsymbol{H})\right]^{-1}\left[(1 - \sqrt[N]{\rho_\infty})\boldsymbol{P}_{n-1,n}(\Delta t\boldsymbol{H}) + 2\sqrt[N]{\rho_\infty}\boldsymbol{P}_{n,n}(\Delta t\boldsymbol{H})\right] := \bar{\boldsymbol{Q}}^{-1}(\Delta t\boldsymbol{H})\bar{\boldsymbol{P}}(\Delta t\boldsymbol{H}). \tag{13}$$

Then, the incremental matrix $\Delta\boldsymbol{S}(\Delta t\boldsymbol{H})$ in Equation (9) becomes the function of $\sqrt[N]{\rho_\infty}$.

The calculation of the convolution integral $\boldsymbol{L}_{\text{ana}}$ in Equation (2) is relatively expensive. Hence, in our work, the vector $\boldsymbol{L}_{\text{ana}}$ is approximated by r-node Gauss–Legendre quadrature method ($r = 1, 2, \dots$), and its expression has the form as

$$\boldsymbol{L}_{\text{num}}(\Delta t) = \frac{\Delta t}{2}\sum_{l=1}^{r} w_l\boldsymbol{A}_{\text{num}}\left[\frac{\Delta t}{2}(1 - \xi_l)\right]\boldsymbol{f}\left[\boldsymbol{y}_{t+\frac{\Delta t}{2}(1+\xi_l)}, t + \frac{\Delta t}{2}(1 + \xi_l)\right]. \tag{14}$$

The explicit expression of which is known for linear systems; hence, together with Equations (12) and (14), the numerical results at discretized time points can be obtained. For nonlinear systems, the values of the state vector $\boldsymbol{y}$ at the quadrature points of $t + (1 + \xi_l)\Delta t/2$ ($l = 1, 2, \dots, r$), which are used in Equation (14), are calculated by the explicit Runge–Kutta methods [3], as follows

$$\begin{cases} \boldsymbol{y}_{t+\Delta t_l} = \boldsymbol{y}_t + \Delta t_l \sum_{i=1}^{s} b_i \boldsymbol{k}_i \\ \boldsymbol{k}_i = \boldsymbol{H}\left(\boldsymbol{y}_t + \Delta t_l \sum_{j=1}^{s} a_{ij}\boldsymbol{k}_j\right) + \boldsymbol{f}\left(\boldsymbol{y}_t + \Delta t_l \sum_{j=1}^{s} a_{ij}\boldsymbol{k}_j, t + c_i \Delta t_l\right) \end{cases}, \Delta t_l = \frac{\Delta t}{2}(1+\xi_l),\ l = 1, 2, \ldots r, \tag{15}$$

where

$$\begin{array}{cc} \boldsymbol{c} & \boldsymbol{A} \\ \boldsymbol{b}^{\mathrm{T}} & \end{array} \rightarrow \begin{array}{ccccc} 0 & 0 & & & \\ c_2 & a_{21} & \ddots & & \\ \vdots & \vdots & \ddots & \ddots & \cdot \\ c_s & a_{s1} & \cdots & a_{s,s-1} & 0 \\ & b_1 & \cdots & \cdots & b_s \end{array} \tag{16}$$

For linear systems, the time integration methods of different orders (or different n) based on the above strategy have unconditional stability, controllable dissipation, and higher-order accuracy, refer to Section 3. Additionally, for the force-free case, the constructed methods can reach computer precision with the increase of m.

For nonlinear systems, the time integration methods produced by the proposed strategy have advantages both in accuracy and efficiency because the responses are arrived at by highly accurate $\boldsymbol{A}_{\mathrm{num}}(\Delta t\boldsymbol{H})$ and $\boldsymbol{L}_{\mathrm{num}}(\Delta t\boldsymbol{H})$, and the Newton iteration method can be avoided.

In the simulations of practical dynamics, the second-order accurate time integration methods, such as the central difference method (CDM) and the TR, are widely utilized. In addition, the fourth-stage fourth-order Runge–Kutta method is also popular. Therefore, in the following, second- and fourth-order accurate schemes based on the present strategy are formulated, and their properties are deliberately discussed in Section 3.

2.1. Second-Order Accurate Scheme

In this case, the generalized Padé approximation with $n = 1$ [48] and the second-order accurate Runge–Kutta method (or named modified Euler method) [3] are employed. Then, from Equation (5), we can read that

$$\boldsymbol{P}_{0,1}(\Delta t\boldsymbol{H}) = \boldsymbol{I}, \boldsymbol{P}_{1,1}(\Delta t\boldsymbol{H}) = \boldsymbol{I} + \frac{1}{2}(\Delta t\boldsymbol{H}) \tag{17}$$

$$\text{and } \boldsymbol{Q}_{0,1}(\Delta t\boldsymbol{H}) = \boldsymbol{I} - (\Delta t\boldsymbol{H}), \boldsymbol{Q}_{1,1}(\Delta t\boldsymbol{H}) = \boldsymbol{I} - \frac{1}{2}(\Delta t\boldsymbol{H}). \tag{18}$$

Substituting Equations (17) and (18) into Equation (4) can lead to

$$\bar{\boldsymbol{P}}(\Delta t\boldsymbol{H}) = (1+\rho_\infty)\boldsymbol{I} + \rho_\infty(\Delta t\boldsymbol{H}) \tag{19}$$

$$\text{and } \bar{\boldsymbol{Q}}(\Delta t\boldsymbol{H}) = (1+\rho_\infty)\boldsymbol{I} - (\Delta t\boldsymbol{H}). \tag{20}$$

With the comparison between Equation (6) and Equations (19) and (20), we can see that

$$\alpha_0 = (1+\rho_\infty), \boldsymbol{S}_1(\Delta t\boldsymbol{H}) = -(\Delta t\boldsymbol{H}) \tag{21}$$

$$\text{and } \beta_0 = (1+\rho_\infty), \boldsymbol{S}_2(\Delta t\boldsymbol{H}) = \rho_\infty(\Delta t\boldsymbol{H}). \tag{22}$$

Then, applying Equations (21) and (22) to Equation (9) can yield the expression of the incremental matrix $\Delta\boldsymbol{S}(\Delta t\boldsymbol{H})$ as follows

$$\Delta\boldsymbol{S}(\Delta t\boldsymbol{H}) = -(1+\rho_\infty)\left[\boldsymbol{I} - (1+\rho_\infty)(\Delta t\boldsymbol{H})^{-1}\right]^{-1}. \tag{23}$$

$\Delta\boldsymbol{S}(\Delta t\boldsymbol{H})$, the highly accurate matrix $\boldsymbol{A}_{\mathrm{num}}(\Delta t\boldsymbol{H})$, can be obtained from Equations (10)–(13). Together with Equation (23) and the Gauss–Legendre quadrature

method, the transient response can be solved for linear systems. For nonlinear systems, here we adopt the modified Euler method to explicitly calculate the values of nonlinear terms $\boldsymbol{f}(\boldsymbol{y}, t)$ at Gauss–Legendre quadrature points. The tableau of the modified Euler method has the form as

$$\begin{array}{cc} \boldsymbol{c} & \boldsymbol{A} \\ & \boldsymbol{b}^{\mathrm{T}} \end{array} \rightarrow \begin{array}{ccc} 0 & 0 & 0 \\ 1 & 1 & 0 \\ & 1/2 & 1/2 \end{array}. \tag{24}$$

2.2. Fourth-Order Accurate Scheme

In this scheme, the generalized Padé approximation with $n = 2$ [48] and the classical four-order Runge–Kutta method [3] are employed. It can be obtained from Equation (5) that

$$\boldsymbol{P}_{1,2}(\Delta t\boldsymbol{H}) = \boldsymbol{I} + \frac{1}{3}(\Delta t\boldsymbol{H}), \boldsymbol{P}_{2,2}(\Delta t\boldsymbol{H}) = \boldsymbol{I} + \frac{1}{2}(\Delta t\boldsymbol{H}) + \frac{1}{12}(\Delta t\boldsymbol{H})^2 \tag{25}$$

$$\text{and } \boldsymbol{Q}_{1,2}(\Delta t\boldsymbol{H}) = \boldsymbol{I} - \frac{2}{3}(\Delta t\boldsymbol{H}) + \frac{1}{6}(\Delta t\boldsymbol{H})^2, \boldsymbol{Q}_{2,2}(\Delta t\boldsymbol{H}) = \boldsymbol{I} - \frac{1}{2}(\Delta t\boldsymbol{H}) + \frac{1}{12}(\Delta t\boldsymbol{H})^2. \tag{26}$$

Substituting Equations (25) and (26) into Equation (4) leads to

$$\bar{\boldsymbol{P}}(\Delta t\boldsymbol{H}) = (1+\rho_\infty)\boldsymbol{I} + \frac{1}{3}(1+2\rho_\infty)(\Delta t\boldsymbol{H}) + \frac{1}{6}\rho_\infty(\Delta t\boldsymbol{H})^2 \tag{27}$$

$$\text{and } \bar{\boldsymbol{Q}}(\Delta t\boldsymbol{H}) = (1+\rho_\infty)\boldsymbol{I} - \frac{1}{3}(2+\rho_\infty)(\Delta t\boldsymbol{H}) + \frac{1}{6}(\Delta t\boldsymbol{H})^2. \tag{28}$$

From this, we can read that

$$\alpha_0 = (1+\rho_\infty), \boldsymbol{S}_1(\Delta t\boldsymbol{H}) = -\frac{1}{3}(2+\rho_\infty)(\Delta t\boldsymbol{H}) + \frac{1}{6}(\Delta t\boldsymbol{H})^2 \tag{29}$$

$$\text{and } \beta_0 = (1+\rho_\infty), \boldsymbol{S}_2(\Delta t\boldsymbol{H}) = \frac{1}{3}(1+2\rho_\infty)(\Delta t\boldsymbol{H}) + \frac{1}{6}\rho_\infty(\Delta t\boldsymbol{H})^2. \tag{30}$$

Then, inserting Equations (29) and (30) into Equation (9) yields the expression of the incremental matrix $\Delta\boldsymbol{S}(\Delta t\boldsymbol{H})$ of the fourth-order scheme, as follows:

$$\Delta\boldsymbol{S}(\Delta t\boldsymbol{H}) = \left\{\boldsymbol{I} + (1+\rho_\infty)\left[-\frac{1}{3}(2+\rho_\infty)\boldsymbol{I} + \frac{1}{6}(\Delta t\boldsymbol{H})\right]^{-1}(\Delta t\boldsymbol{H})^{-1}\right\}^{-1}\left[-\frac{1}{3}(2+\rho_\infty)\boldsymbol{I} + \frac{1}{6}(\Delta t\boldsymbol{H})\right]^{-1}\left[(1+\rho_\infty)\boldsymbol{I} + \frac{1}{6}(\rho_\infty - 1)(\Delta t\boldsymbol{H})\right]. \tag{31}$$

One can find that, for the case of $\rho_\infty = 1$, Equation (31) turns into

$$\Delta\boldsymbol{S}(\Delta t\boldsymbol{H}) = 2\left\{\boldsymbol{I} + 2\left[-\boldsymbol{I} + \frac{1}{6}(\Delta t\boldsymbol{H})\right]^{-1}(\Delta t\boldsymbol{H})^{-1}\right\}^{-1}\left[-\boldsymbol{I} + \frac{1}{6}(\Delta t\boldsymbol{H})\right]^{-1}, \tag{32}$$

and for the case of $\rho_\infty = 0$, Equation (31) becomes

$$\Delta\boldsymbol{S}(\Delta t\boldsymbol{H}) = \left\{\boldsymbol{I} + \left[-\frac{2}{3}\boldsymbol{I} + \frac{1}{6}(\Delta t\boldsymbol{H})\right]^{-1}(\Delta t\boldsymbol{H})^{-1}\right\}^{-1}\left[-\frac{2}{3}\boldsymbol{I} + \frac{1}{6}(\Delta t\boldsymbol{H})\right]^{-1}\left[\boldsymbol{I} - \frac{1}{6}(\Delta t\boldsymbol{H})\right]. \tag{33}$$

It can be concluded from Equations (31)–(33) that the computations of the fourth-order scheme with $\rho_\infty = 1$ are the lowest. The classical fourth-order Runge–Kutta method [3] is utilized in the present scheme to compute nonlinear function $\boldsymbol{f}(\boldsymbol{y}, t)$ at Gauss–Legendre

quadrature points to avoid the loss-of-accuracy order and the tableau of the Runge–Kutta method is

$$\begin{array}{c|cccc} \boldsymbol{c} & \boldsymbol{A} & & & \\ & \boldsymbol{b}^{\mathrm{T}} & & & \end{array} \rightarrow \begin{array}{c|cccc} 0 & & & & \\ 1/2 & 1/2 & & & \\ 1/2 & 0 & 1/2 & & \\ 1 & 0 & 0 & 1 & \\ & 1/6 & 1/3 & 1/3 & 1/6 \end{array}. \tag{34}$$

3. Numerical Properties Analysis

The basic idea of the proposed strategy has been described in the last section, and two schemes are formulated, which are second-order accurate and fourth-order accurate. In this section, the spectral characteristics, convergence rates, and overshoot characteristics for both undamped and damped systems are investigated. Additionally, the critical value of m is noted as m_{cr}, and ensures that the constructed matrix $\boldsymbol{A}_{\mathrm{num}}(\Delta t\boldsymbol{H})$ can be calculated with up to computer precision, which is also discussed below.

Spectral analysis has been widely employed in the evaluation of the stability, accuracy, and dissipation characteristics of time integration methods. In spectral analysis, owing to the mode superposition principle, it is common and enough to consider a single degree-of-freedom Equation [1]

$$\ddot{x} + 2\xi\omega\dot{x} + \omega^2 x = f(t), \tag{35}$$

where ξ is the damping ratio, and ω is the natural frequency. The equivalent first-order differential equation for the free-force case [52] has the following form as

$$\dot{\boldsymbol{y}} = \begin{bmatrix} 0 & 1 \\ -\omega^2 & -2\xi\omega \end{bmatrix} \boldsymbol{y},\ \boldsymbol{y} = \begin{bmatrix} x \\ \dot{x} \end{bmatrix}, \tag{36}$$

from which we can find that

$$\boldsymbol{H} = \begin{bmatrix} 0 & 1 \\ -\omega^2 & -2\xi\omega \end{bmatrix}. \tag{37}$$

Applying Equations (3)–(5) to Equation (36) generates

$$\begin{bmatrix} x_{t+\Delta t} \\ \dot{x}_{t+\Delta t} \end{bmatrix} = \bar{\boldsymbol{Q}}^{-1}(\Delta t\boldsymbol{H})\bar{\boldsymbol{P}}(\Delta t\boldsymbol{H}) \begin{bmatrix} x_t \\ \dot{x}_t \end{bmatrix} := \boldsymbol{A}_{\mathrm{num}}(\Delta t\boldsymbol{H}) \begin{bmatrix} x_t \\ \dot{x}_t \end{bmatrix}. \tag{38}$$

The characteristic polynomial [1] of the transfer matrix $\boldsymbol{A}_{\mathrm{num}}$ is

$$\lambda^2 - A_1\lambda + A_2 = 0, \tag{39}$$

where $A_1 = \mathrm{tr}(\boldsymbol{A}_{\mathrm{num}})$ and $A_2 = \det(\boldsymbol{A}_{\mathrm{num}})$, and the two eigenvalues can be written as the form of $\lambda_{1,2} = a \pm \mathrm{i}b$, in which $\mathrm{i} = \sqrt{-1}$. The definition of the spectral radius [1] is

$$\rho = \max\{|\lambda_1|, |\lambda_2|\}, \tag{40}$$

which can be used to analyze the stability and dissipation characteristics of time integration methods. Numerical damping ratio $\bar{\xi}$ [1] and period elongation (PE) [1] can evaluate the amplitude and phase accuracy of time integration methods in the low-frequency range, and their definitions are

$$\bar{\xi} = -\frac{\ln(\rho)}{2\bar{\tau}} \text{ and } \mathrm{PE} = \frac{\tau}{\bar{\tau}} - 1, \tag{41}$$

where $\tau = \omega\Delta t$ and $\bar{\tau} = \arctan(b/a)$. In the following, the above theory given in Equations (35)–(41) is used to analyze the fundamental numerical properties of the two schemes provided in Section 2. In this work, the time integration methods based on the proposed strategy are named Accurate-Efficient-Conservative/Dissipative-Method-n (AEC/DMn), in which n stands for polynomials of degree in the numerator or denominator of the generalized Padé approximation. The non-dissipative AECMn (ρ_∞ = 1) can keep all

information of a dynamic system, while the dissipative AEDMn ($0 \leq \rho_\infty < 1$) can filter out the high-frequency modes.

3.1. Stability, Dissipation, and Accuracy of the Second-Order Scheme

3.1.1. Spectral Characteristics

The spectral radius of AEC/DM1 versus τ for the undamped case ($\xi = 0$) is plotted in Figure 1, in which one can see that (a) for linear systems, the AEC/DM1 is unconditionally stable, satisfying $0 \leq \rho_\infty \leq 1$, and the amount of its high-frequency dissipation can be exactly controlled via ρ_∞. (b) Additionally, with the increase of m, the low-frequency range, where the spectral radius trends to 1, becomes wider and preserves more low-frequency modes.

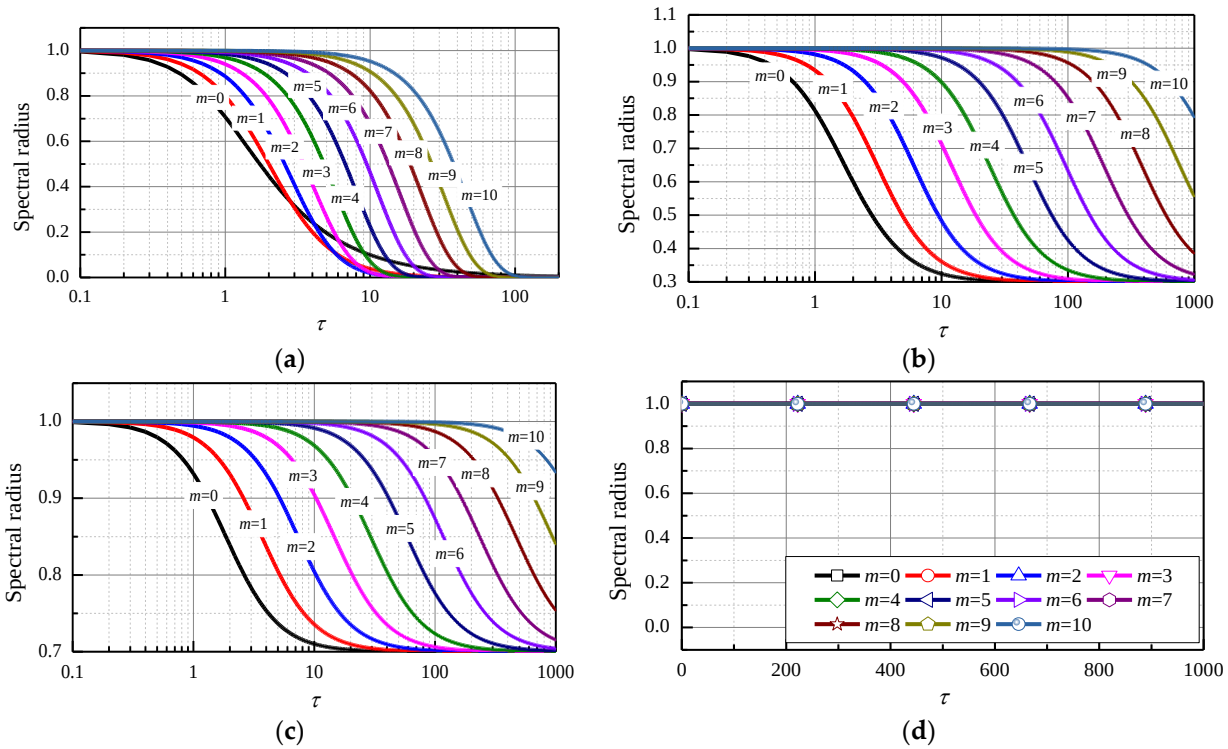

Figure 1. Spectral radius of the AEC/DM1 versus τ for the undamped case: (**a**) AEDM1, $\rho_\infty = 0$; (**b**) AEDM1, $\rho_\infty = 0.3$; (**c**) AEDM1, $\rho_\infty = 0.7$; and (**d**) AECM1, $\rho_\infty = 1$.

The AEDM1 ($\rho_\infty = 0$) and AECM1 ($\rho_\infty = 1$), which are the representative schemes, are considered below for analyzing the amplitude and phase accuracy of the present scheme. Amplitude and period errors of the AEDM1 ($\rho_\infty = 0$) and AECM1 ($\rho_\infty = 1$) versus τ for the undamped case are shown in Figures 2 and 3, respectively, in which it can be seen that (a) with the increase in m, both the amplitude and period errors can be simultaneously decreased; (b) for the same m, the non-dissipative scheme and the dissipative schemes almost have the same phase accuracy, implying that the numerical dissipation mainly affects the amplitude accuracy of the AEC/DM1.

The spectral radii ρ and absolute values of (ρ-ρ_{exact}) of the AEC/DM1 for the damped case ($\xi = 0.5$) are shown in Figures 4–6, in which $\rho_{\text{exact}} = \exp(-\xi\tau)$ [52]. It follows that: (a) With the increase of m, the numerical spectral radius approaches the analytical one; (b) Among the low-frequency range, the accuracy of the AECM1 is higher than that of the AEDM1; (c) For smaller m, because the AECM1 cannot provide numerical dissipation, their spectral radii do not agree well with analytical one in the high-frequency range ($\tau > 10$).

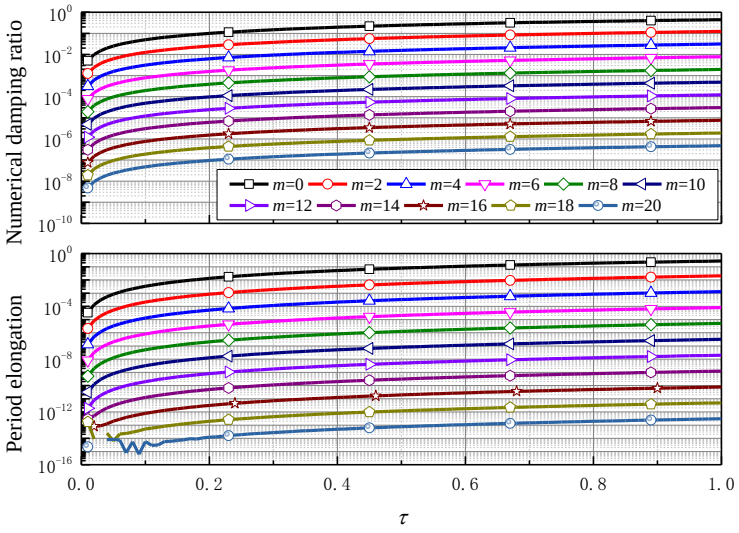

Figure 2. Numerical damping ratio and period elongation of the AEDM1 ($\rho_\infty = 0$) versus τ for the undamped case.

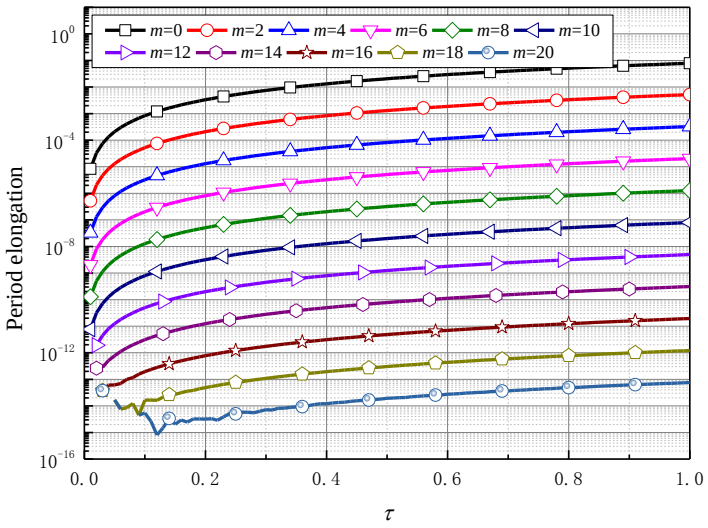

Figure 3. Period elongation of the AECM1 ($\rho_\infty = 1$) versus τ for the undamped case.

3.1.2. Rounding Errors

As well known, the accuracy of numerical results depends on the truncation error, which can be reduced by decreasing step size or increasing m. However, when m is large enough, all significant digits of the incremental matrix reserved by the computer are completely accurate. At this time, the truncation error does not exist, and the rounding error of the computer dominates, where further increasing m cannot further improve accuracy. That is to say, there exists a critical value of m, denoted as m_{cr}. When $m < m_{\mathrm{cr}}$, the truncation error dominates, and increasing m can improve accuracy, but when $m \geq m_{\mathrm{cr}}$, the rounding error dominates, and increasing m cannot improve accuracy further. From the phase accuracy analysis shown in Figures 2 and 3, one can find that the value of ρ_∞ has a slight influence on the phase accuracy of the proposed methods; therefore, we only determine m_{cr} for the AECM1.

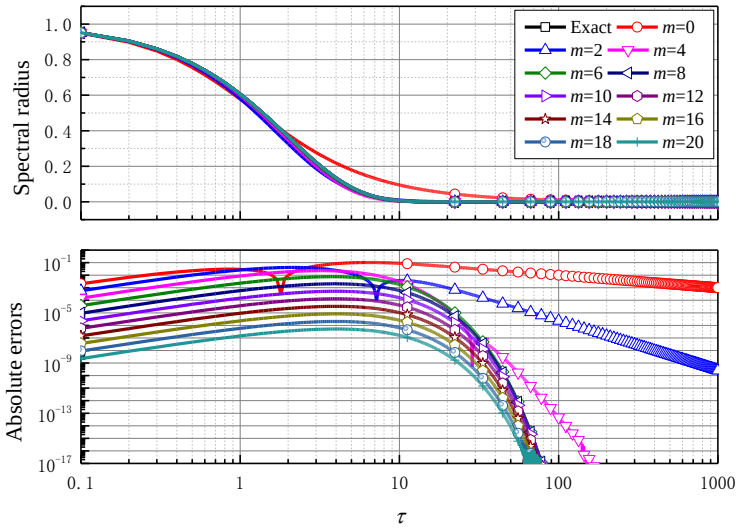

Figure 4. Spectral radius of the AEDM1 ($\rho_\infty = 0$) versus τ for the damped case ($\xi = 0.5$).

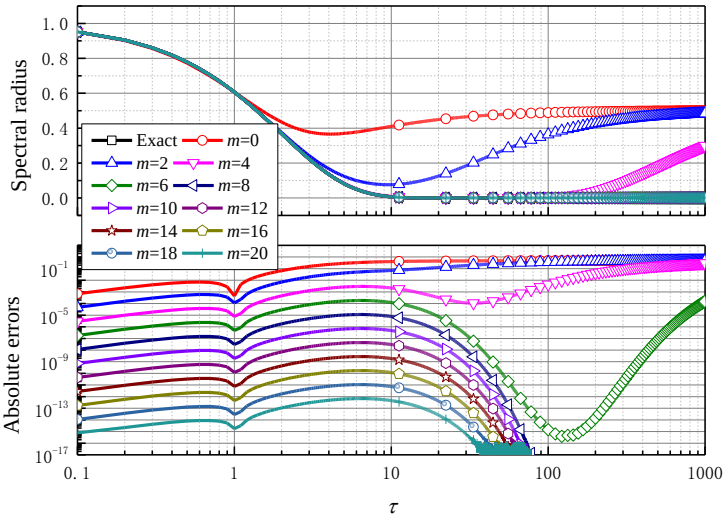

Figure 5. Spectral radius of the AEDM1 ($\rho_\infty = 0.5$) versus τ for the damped case ($\xi = 0.5$).

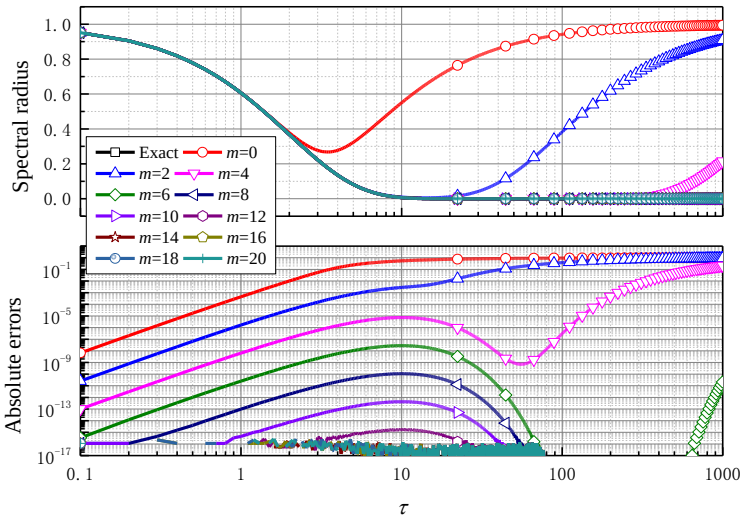

Figure 6. Spectral radius of the AECM1 versus τ for the damped case ($\xi = 0.5$).

The transfer matrix of the AEC/DM1 has the form as

$$\boldsymbol{A}_{\text{num}}(\Delta t\boldsymbol{H}) = \begin{bmatrix} A_{11} & A_{12} \\ A_{21} & A_{22} \end{bmatrix}, \tag{42}$$

which elements for the case of $\rho_\infty = 1$ have the forms as

$$A_{\text{num},11} = 1 - \frac{\Delta t_N^2\omega^2}{2} + \frac{\xi\Delta t_N^3\omega^3}{2} + \frac{\Delta t_N^4\omega^4}{8} - \frac{\xi^2\Delta t_N^4\omega^4}{2} - \frac{\xi\Delta t_N^5\omega^5}{4} + \frac{\xi^3\Delta t_N^5\omega^5}{2}, \tag{43}$$

$$A_{\text{num},12} = \Delta t_N - \xi\Delta t_N^2\omega - \frac{\Delta t_N^3\omega^2}{4} + \xi^2\Delta t_N^3\omega^2 + \frac{\xi\Delta t_N^4\omega^3}{2} - \xi^3\Delta t_N^4\omega^3 + \frac{\Delta t_N^5\omega^4}{16} - \frac{3\xi^2\Delta t_N^5\omega^4}{4} + \xi^4\Delta t_N^5\omega^4, \tag{44}$$

$$A_{\text{num},21} = -\Delta t_N\omega^2\left(1 - \xi\Delta t_N\omega - \frac{1}{4}\Delta t_N^2\omega^2 + \xi^2\Delta t_N^2\omega^2 + \frac{1}{2}\xi\Delta t_N^3\omega^3 - \xi^3\Delta t_N^3\omega^3 + \frac{1}{16}\Delta t_N^4\omega^4 - \frac{3}{4}\xi^2\Delta t_N^4\omega^4 + \xi^4\Delta t_N^4\omega^4\right), \tag{45}$$

$$\text{and } A_{\text{num},22} = 1 - 2\xi\Delta t_N\omega - \frac{\Delta t_N^2\omega^2}{2} + 2\xi^2\Delta t_N^2\omega^2 + \xi\Delta t_N^3\omega^3 - 2\xi^3\Delta t_N^3\omega^3 + \frac{\Delta t_N^4\omega^4}{8} - \frac{3\xi^2\Delta t_N^4\omega^4}{2} + 2\xi^4\Delta t_N^4\omega^4 - \frac{3\xi\Delta t_N^5\omega^5}{8} + 2\xi^3\Delta t_N^5\omega^5 - 2\xi^5\Delta t_N^5\omega^5. \tag{46}$$

Then, the corresponding elements of the incremental matrix are

$$S_{\text{num},11} = A_{\text{num},11} - 1, \tag{47}$$

$$S_{\text{num},12} = A_{\text{num},12}, \tag{48}$$

$$S_{\text{num},21} = A_{\text{num},21}, \tag{49}$$

$$\text{and } S_{\text{num},22} = A_{\text{num},22} - 1. \tag{50}$$

The analytical sub-step transfer matrix based on Taylor series expansion has the same form as that of the numerical one shown in Equation (42), but its elements turn into

$$A_{\text{ana},11} = 1 - \frac{\Delta t_N^2\omega^2}{2} + \frac{\xi\Delta t_N^3\omega^3}{3} + \frac{\Delta t_N^4\omega^4}{24} - \frac{\xi^2\Delta t_N^4\omega^4}{6} - \frac{\xi\Delta t_N^5\omega^5}{30} + \frac{\xi^3\Delta t_N^5\omega^5}{15} - \frac{\Delta t_N^6\omega^6}{720} + \frac{\xi^2\Delta t_N^6\omega^6}{60} - \frac{\xi^4\Delta t_N^6\omega^6}{45} + \frac{\xi\Delta t_N^7\omega^7}{840} - \frac{2\xi^3\Delta t_N^7\omega^7}{315} + \frac{2\xi^5\Delta t_N^7\omega^7}{315} + \frac{\Delta t_N^8\omega^8}{40320} - \cdots, \tag{51}$$

$$A_{\text{ana},12} = \Delta t_N\left(1 - \xi\Delta t_N\omega - \frac{1}{6}\Delta t_N^2\omega^2 + \frac{2}{3}\xi^2\Delta t_N^2\omega^2 + \frac{1}{6}\xi\Delta t_N^3\omega^3 - \frac{1}{3}\xi^3\Delta t_N^3\omega^3 + \frac{1}{120}\Delta t_N^4\omega^4 - \frac{1}{10}\xi^2\Delta t_N^4\omega^4 + \frac{2}{15}\xi^4\Delta t_N^4\omega^4 - \frac{1}{120}\xi\Delta t_N^5\omega^5 + \frac{2}{45}\xi^3\Delta t_N^5\omega^5 - \frac{2}{45}\xi^5\Delta t_N^5\omega^5 - \frac{1}{5040}\Delta t_N^6\omega^6 + \frac{1}{210}\xi^2\Delta t_N^6\omega^6 - \frac{1}{63}\xi^4\Delta t_N^6\omega^6 + \frac{4}{315}\xi^6\Delta t_N^6\omega^6 - \cdots\right), \tag{52}$$

$$A_{\text{ana},21} = -\Delta t_N\omega^2\left(1 - \xi\Delta t_N\omega - \frac{1}{6}\Delta t_N^2\omega^2 + \frac{2}{3}\xi^2\Delta t_N^2\omega^2 + \frac{1}{6}\xi\Delta t_N^3\omega^3 - \frac{1}{3}\xi^3\Delta t_N^3\omega^3 + \frac{1}{120}\Delta t_N^4\omega^4 - \frac{1}{10}\xi^2\Delta t_N^4\omega^4 + \frac{2}{15}\xi^4\Delta t_N^4\omega^4 - \frac{1}{120}\xi\Delta t_N^5\omega^5 + \frac{2}{45}\xi^3\Delta t_N^5\omega^5 - \frac{2}{45}\xi^5\Delta t_N^5\omega^5 - \frac{1}{5040}\Delta t_N^6\omega^6 + \frac{1}{210}\xi^2\Delta t_N^6\omega^6 - \frac{1}{63}\xi^4\Delta t_N^6\omega^6 + \frac{4}{315}\xi^6\Delta t_N^6\omega^6 - \cdots\right), \tag{53}$$

$$\text{and } A_{\text{ana},22} = 1 - 2\xi\Delta t_N\omega - \frac{\Delta t_N^2\omega^2}{2} + 2\xi^2\Delta t_N^2\omega^2 + \frac{2\xi\Delta t_N^3\omega^3}{3} - \frac{4\xi^3\Delta t_N^3\omega^3}{3} + \frac{\Delta t_N^4\omega^4}{24} - \frac{\xi^2\Delta t_N^4\omega^4}{2} + \frac{2\xi^4\Delta t_N^4\omega^4}{3} - \frac{\xi\Delta t_N^5\omega^5}{20} + \frac{4\xi^3\Delta t_N^5\omega^5}{15} - \frac{4\xi^5\Delta t_N^5\omega^5}{15} - \frac{\Delta t_N^6\omega^6}{720} + \frac{\xi^2\Delta t_N^6\omega^6}{30} - \frac{\xi^4\Delta t_N^6\omega^6}{9} + \frac{4\xi^6\Delta t_N^6\omega^6}{45} + \cdots. \tag{54}$$

The undamped case ($\xi = 0$) is investigated first. By comparing Equations (43)–(46) with Equations (51)–(54), we have the relative sizes between four truncation terms and four main terms in $S(\Delta t_N)$ as

$$\begin{cases} \left|\frac{\chi_{\text{truncation}}(A_{\text{num},11} - A_{\text{ana},11})}{\chi_{\text{main}}(S_{\text{num},11})}\right| = \left|\frac{\Delta t_N^2\omega^2/8 - \Delta t_N^2\omega^2/24}{\Delta t_N^2\omega^2/2}\right| = \left|\frac{\Delta t_N^2\omega^2}{6}\right| \\ \left|\frac{\chi_{\text{truncation}}(A_{\text{num},12} - A_{\text{ana},12})}{\chi_{\text{main}}(S_{\text{num},12})}\right| = \left|\frac{\Delta t_N^3\omega^2/6 - \Delta t_N^3\omega^2/4}{\Delta t_N}\right| = \left|\frac{\Delta t_N^2\omega^2}{12}\right| \\ \left|\frac{\chi_{\text{truncation}}(A_{\text{num},21} - A_{\text{ana},21})}{\chi_{\text{main}}(S_{\text{num},21})}\right| = \left|\frac{\Delta t_N^3\omega^4/6 - \Delta t_N^3\omega^4/4}{\Delta t_N\omega^2}\right| = \left|\frac{\Delta t_N^2\omega^2}{12}\right| \\ \left|\frac{\chi_{\text{truncation}}(A_{\text{num},22} - A_{\text{ana},22})}{\chi_{\text{main}}(S_{\text{num},22})}\right| = \left|\frac{\Delta t_N^2\omega^2/8 - \Delta t_N^2\omega^2/24}{\Delta t_N^2\omega^2/2}\right| = \left|\frac{\Delta t_N^2\omega^2}{6}\right| \end{cases}. \tag{55}$$

Then, the truncation errors can be eliminated if

$$\max\left\{\left|\frac{\Delta t_N^2\omega^2}{6}\right|, \left|\frac{\Delta t_N^2\omega^2}{12}\right|, \left|\frac{\Delta t_N^2\omega^2}{12}\right|, \left|\frac{\Delta t_N^2\omega^2}{6}\right|\right\} = \frac{\Delta t^2\omega^2}{6 \times 2^{2m}} \le \varepsilon,\ \varepsilon = 10^{-16}. \tag{56}$$

From this, the critical value of m for the undamped case can be obtained as

$$m_{\mathrm{cr}} = \frac{\log\left(\Delta t^2 \omega^2 / 6\varepsilon\right)}{2\log(2)}, \ \varepsilon = 10^{-16}. \tag{57}$$

In the following, the performances of the AEC/DM1 in dealing with rounding errors are discussed. The undamped case of Equation (35) is considered first, in which $\xi = 0$, $\omega = \pi$, $x_0 = 1$, and $\dot{x}_0 = 1$; $\Delta t = 1$ and $\Delta t_N = 1/N$ are used in the AEC/DM1 and TR, respectively. The absolute errors in displacement, velocity, and acceleration of the AECM1 and TR are drawn in Figure 7, and one can see that: (a) When $m > m_{\mathrm{cr}} = 27$ is achieved from Equation (57), the absolute errors of the AECM1 trends with computer precision; (b) With the increase of m, the accuracy of TR increases for the case of $m < 20$, and then its accuracy begins to decline when $m > 20$ due to the rounding errors. Figure 8 plots the relative errors of the two methods for the damped case, in which $\xi = 0.5$, $\omega = 2\pi$, $x_0 = 1$, and $\dot{x}_0 = 0$, and it follows that the accuracy of the AECM1 has no considerable variation when $m > m_{\mathrm{cr}} = 27$. Therefore, one can conclude that the selection of m_{cr} can only consider the undamped case. The m_{cr} corresponding to different $\omega\Delta t$ is given in Table 2, in which one can find that with the increase of $\omega\Delta t$, the m_{cr} becomes larger.

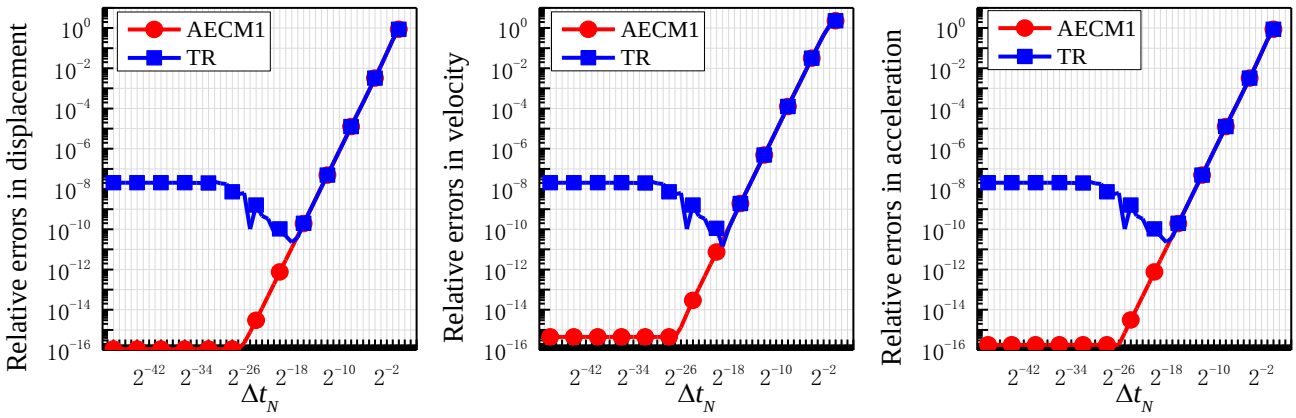

Figure 7. Relative errors in displacement, velocity, and acceleration of the AECM1 for the case of $\xi = 0$ and $f(t) = 0$.

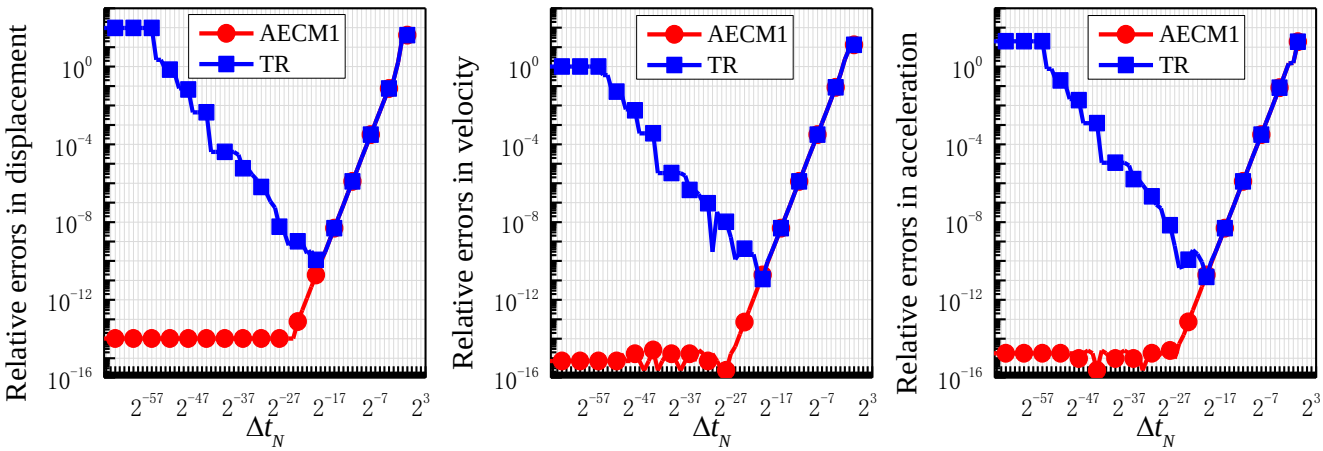

Figure 8. Relative errors in displacement, velocity, and acceleration of the AECM1 for the case of $\xi = 0.5$ and $f(t) = 0$.

Table 2. The critical value of m of the AECM1 for different $\omega\Delta t$.

$\omega\Delta t$	0.01	0.1	1	10	20	50	100	1000	10,000
m_{cr}	19	22	26	29	30	31	32	36	39

At last, the selections of Gauss–Legendre points are discussed below. The standard SDOF test equation given in Equation (35) is considered here, and the $\xi = 2/\sqrt{5}$, $\omega = \sqrt{5}$, $x_0 = 57/65$, $\dot{x}_0 = 2/65$, and $f(t) = \sin(2t)$ are used. The absolute errors of the AECM1 and the TR are compared in Figure 9, in which one can see that: (a) The AECM1 has the same convergence rates with the second-order-accurate TR before $m < 22$; (b) Due to the rounding errors, the accuracy of the TR begins to decrease after $m \geq 23$; (c) The accuracy of the AECM1 trends to constants with the decrease in time-step size, and the accuracy of the AECM1 with four Gauss–Legendre nodes is close to computer precision after $m > m_{\mathrm{cr}} = 23$ is achieved from Equation (57). Therefore, four Gauss–Legendre nodes are suggested for the AEC/DM1.

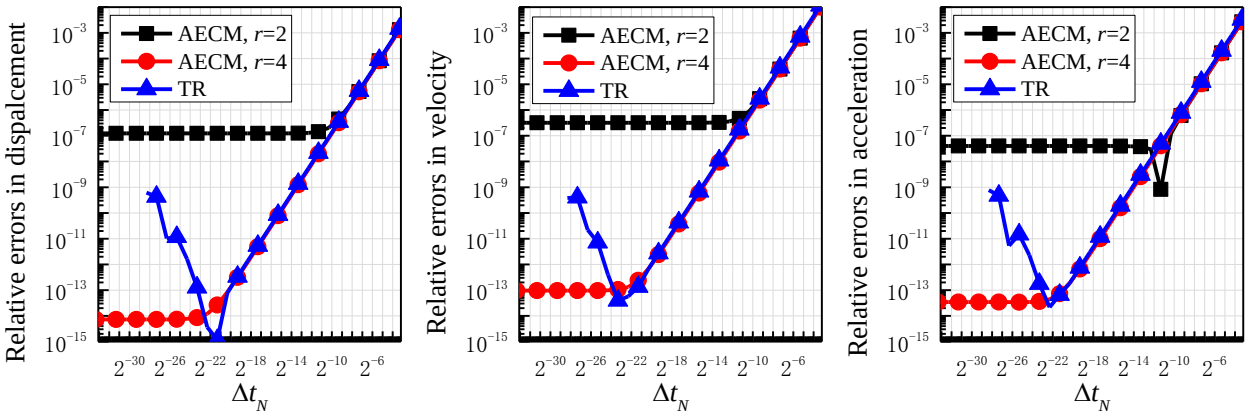

Figure 9. Relative errors in displacement, velocity, and acceleration of the AECM1 for the case of $\xi = 2/\sqrt{5}$) and $f(t) = \sin(2t)$ (r represents number of Gauss–Legendre nodes).

3.2. Stability, Dissipation, and Accuracy of the Fourth-Order Scheme

3.2.1. Spectral Characteristics

Figure 10 plots the spectral radius of AEC/DM2 versus τ for the undamped case, in which one can see that: (a) Compared with the second-order AEC/DM1, the range wherein spectral radius trending to one can rapidly widen with the increase of m (or increasing accuracy order can keep more low-frequency information); (b) Such as in the AEC/DM1, the amount of numerical dissipation of the AEC/DM2 can be exactly adjusted by ρ_∞.

Amplitude and period accuracy of the AEDM2 ($\rho_\infty = 0$) and AECM2 versus τ for the undamped case are shown in Figures 11 and 12, respectively. It can be seen that: (a) With the increase in m, the amplitude and period errors can be simultaneously decreased; (b) From the comparison between Figures 2 and 11, one can find that the accuracy, including amplitude and phase of the AEDM2, is far higher than that of the AEDM1 ($\rho_\infty = 0$); (c) One can observe by comparing Figures 3 and 12 that the AECM2 has a considerable phase advantage compared with the AECM1; (d) For the same m, the phase accuracy of the non-dissipative scheme and the dissipative schemes are nearly the same, implying that m mainly affect the amplitude accuracy of the AEC/DM2.

The spectral radii of the AEC/DM2 for the damped case are discussed here, and from Figures 13–15, the conclusions for the AEC/DM1 hold for the AEC/DM2. However, with the same m, the absolute errors of the AEC/DM2 are smaller than those of AEC/DM1 for the damped case.

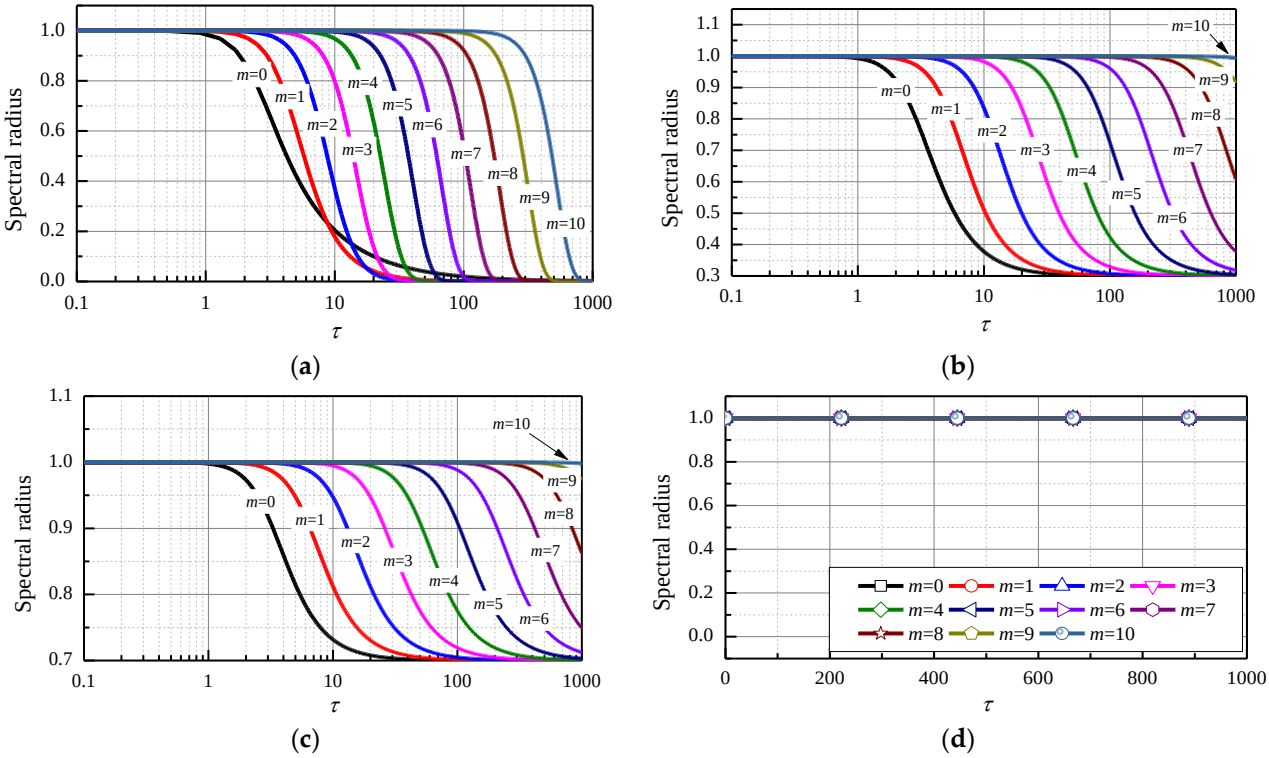

Figure 10. Spectral radius of the AEC/DM2 versus τ for the undamped case: (**a**) AEDM2, $\rho_\infty = 0$; (**b**) AEDM2, $\rho_\infty = 0.3$; (**c**) AEDM2, $\rho_\infty = 0.7$; and (**d**) AECM2, $\rho_\infty = 1$.

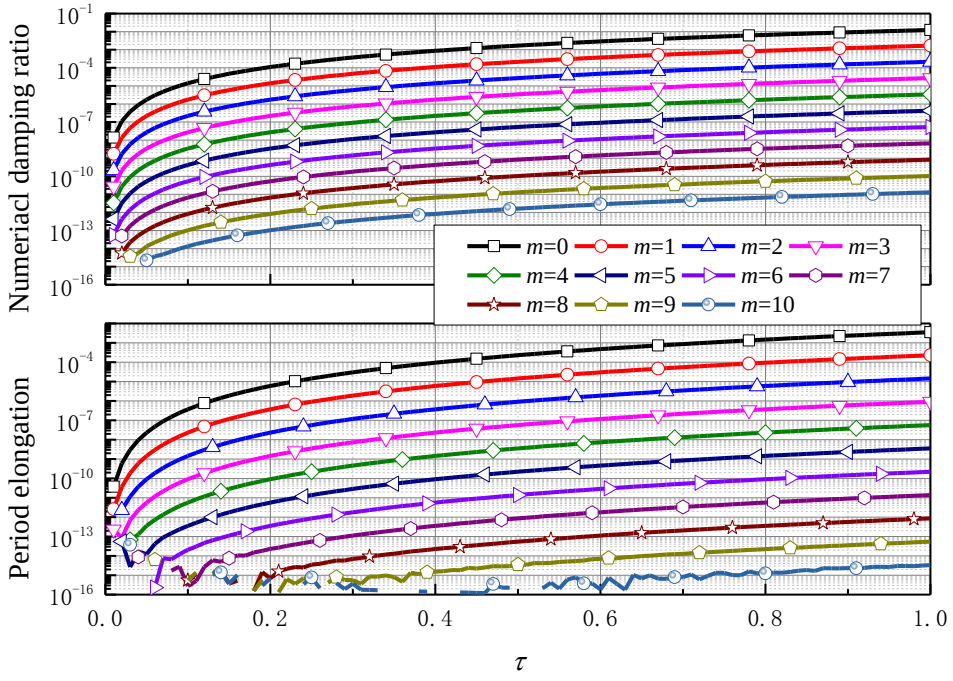

Figure 11. Numerical damping ratio and period elongation of the AEC/DM2 ($\rho_\infty = 0$) versus τ for the undamped case.

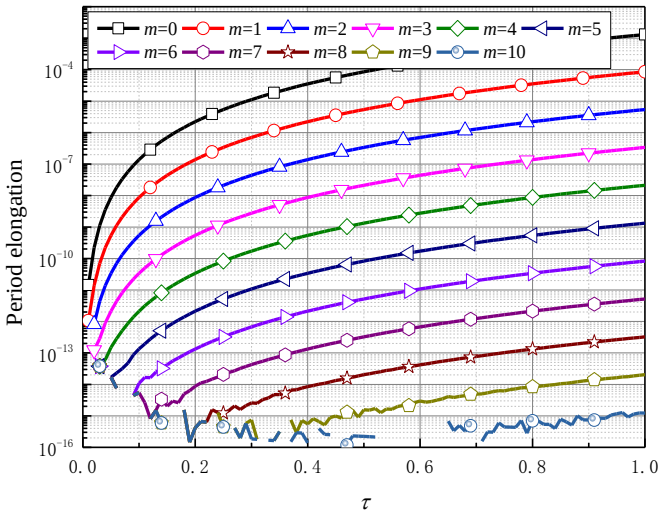

Figure 12. Period elongation of the AEC/DM2 ($\rho_\infty = 1$) versus τ for the undamped case.

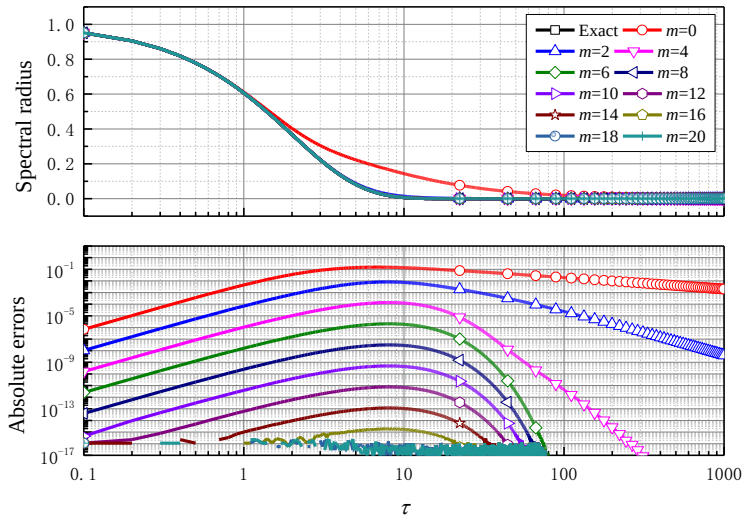

Figure 13. Spectral radius of the AEC/DM2 ($\rho_\infty = 0$) versus τ for the damped case.

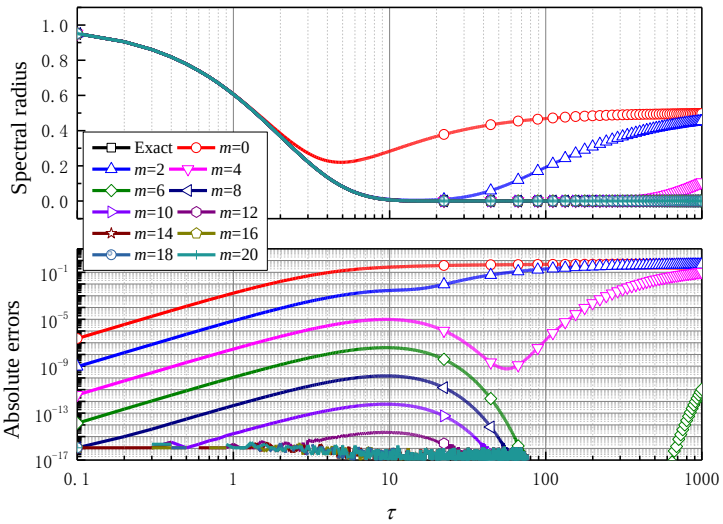

Figure 14. Spectral radius of the AEC/DM2 ($\rho_\infty = 0.5$) versus τ for the damped case.

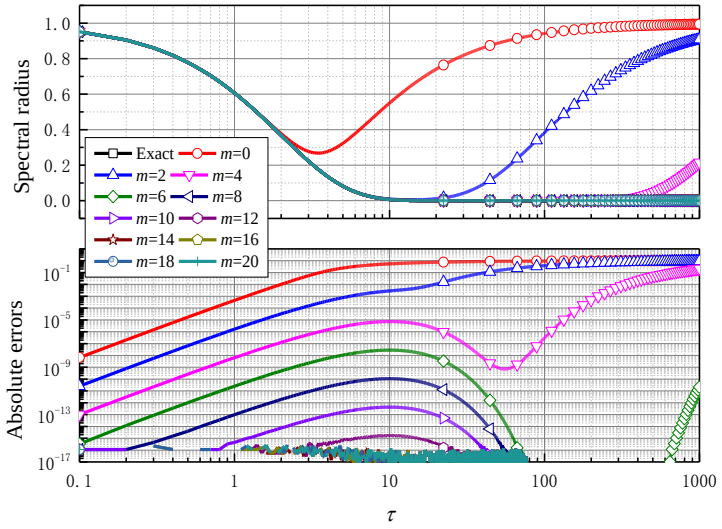

Figure 15. Spectral radius of the AEC/DM2 ($\rho_\infty = 1$) versus τ for the damped case.

3.2.2. Rounding Errors

It can be found from Figures 11 and 12 that, for the AEC/DM2, the effect of numerical dissipation on phase accuracy can be omitted. Thus, in the following, only the critical m of the AECM2 is investigated. The elements of the numerical transfer matrix of the AECM2 have the forms as

$$A_{\text{num},11} = 1 - \frac{\Delta t_N^2\omega^2}{2} + \frac{\xi\Delta t_N^3\omega^3}{3} + \frac{\Delta t_N^4\omega^4}{24} - \frac{\xi^2\Delta t_N^4\omega^4}{6} - \frac{\xi\Delta t_N^5\omega^5}{36} + \frac{\xi^3\Delta t_N^5\omega^5}{18} - \frac{\xi\Delta t_N^7\omega^7}{288} + \frac{\xi^3\Delta t_N^7\omega^7}{54} - \frac{\xi^5\Delta t_N^7\omega^7}{54} - \frac{\Delta t_N^8\omega^8}{3456} - \cdots, \tag{58}$$

$$A_{\text{num},12} = \Delta t_N\left(1 - \xi\Delta t_N\omega - \frac{1}{6}\Delta t_N^2\omega^2 + \frac{2}{3}\xi^2\Delta t_N^2\omega^2 + \frac{1}{6}\xi\Delta t_N^3\omega^3 - \frac{1}{3}\xi^3\Delta t_N^3\omega^3 + \frac{1}{144}\Delta t_N^4\omega^4 - \frac{1}{12}\xi^2\Delta t_N^4\omega^4 + \frac{1}{9}\xi^4\Delta t_N^4\omega^4 + \frac{1}{1728}\Delta t_N^6\omega^6 - \frac{1}{72}\xi^2\Delta t_N^6\omega^6 + \frac{5}{108}\xi^4\Delta t_N^6\omega^6 - \frac{1}{27}\xi^6\Delta t_N^6\omega^6 - \frac{1}{432}\xi\Delta t_N^7\omega^7\right), \tag{59}$$

$$A_{\text{num},21} = -\Delta t_N\omega^2\left(1 - \xi\Delta t_N\omega - \frac{1}{6}\Delta t_N^2\omega^2 + \frac{2}{3}\xi^2\Delta t_N^2\omega^2 + \frac{1}{6}\xi\Delta t_N^3\omega^3 - \frac{1}{3}\xi^3\Delta t_N^3\omega^3 + \frac{1}{144}\Delta t_N^4\omega^4 - \frac{1}{12}\xi^2\Delta t_N^4\omega^4 + \frac{1}{9}\xi^4\Delta t_N^4\omega^4 + \frac{1}{1728}\Delta t_N^6\omega^6 - \frac{1}{72}\xi^2\Delta t_N^6\omega^6 + \frac{5}{108}\xi^4\Delta t_N^6\omega^6 - \frac{1}{27}\xi^6\Delta t_N^6\omega^6 - \frac{1}{432}\xi\Delta t_N^7\omega^7\right), \text{ and} \tag{60}$$

$$A_{\text{num},22} = 1 - 2\xi\Delta t_N\omega - \frac{\Delta t_N^2\omega^2}{2} + 2\xi^2\Delta t_N^2\omega^2 + \frac{2\xi\Delta t_N^3\omega^3}{3} - \frac{4\xi^3\Delta t_N^3\omega^3}{3} + \frac{\Delta t_N^4\omega^4}{24} - \frac{\xi^2\Delta t_N^4\omega^4}{2} + \frac{2\xi^4\Delta t_N^4\omega^4}{3} - \frac{\xi\Delta t_N^5\omega^5}{24} + \frac{2\xi^3\Delta t_N^5\omega^5}{9} - \frac{2\xi^5\Delta t_N^5\omega^5}{9} - \frac{\xi\Delta t_N^7\omega^7}{216} + \frac{5\xi^3\Delta t_N^7\omega^7}{108} - \frac{\xi^5\Delta t_N^7\omega^7}{9} + \frac{2\xi^7\Delta t_N^7\omega^7}{27} - \frac{\Delta t_N^8\omega^8}{3456}. \tag{61}$$

It can be concluded from Section 3.1 that the physical damping has slight effects on the values of m_{cr}; thus, only the undamped case ($\xi = 0$) is considered for the present scheme. By comparing Equation (58)–(61) with Equation (51)–(54), we have the relative sizes between four truncation terms and four main terms in $S(\Delta t_N)$ by

$$\begin{cases} \left|\frac{\chi_{\text{truncation}}(A_{\text{num},11}-A_{\text{ana},11})}{\chi_{\text{main}}(S_{\text{num},11})}\right| = \left|\frac{\Delta t_N^6\omega^6/720}{\Delta t_N^2\omega^2/2}\right| = \left|\frac{\Delta t_N^4\omega^4}{360}\right| \\ \left|\frac{\chi_{\text{truncation}}(A_{\text{num},12}-A_{\text{ana},12})}{\chi_{\text{main}}(S_{\text{num},12})}\right| = \left|\frac{\Delta t_N^3\omega^4/144-\Delta t_N^5\omega^4/120}{\Delta t_N}\right| = \left|\frac{\Delta t_N^4\omega^4}{720}\right| \\ \left|\frac{\chi_{\text{truncation}}(A_{\text{num},21}-A_{\text{ana},21})}{\chi_{\text{main}}(S_{\text{num},21})}\right| = \left|\frac{\Delta t_N^3\omega^6/144-\Delta t_N^5\omega^6/120}{\Delta t_N\omega^2}\right| = \left|\frac{\Delta t_N^4\omega^4}{720}\right| \\ \left|\frac{\chi_{\text{truncation}}(A_{\text{num},22}-A_{\text{ana},22})}{\chi_{\text{main}}(S_{\text{num},22})}\right| = \left|\frac{\Delta t_N^6\omega^6/720}{\Delta t_N^2\omega^2/2}\right| = \left|\frac{\Delta t_N^4\omega^4}{360}\right| \end{cases}. \tag{62}$$

Then, the truncation error can be eliminated if

$$\max\left\{\left|\frac{\Delta t_N^4\omega^4}{360}\right|, \left|\frac{\Delta t_N^4\omega^4}{720}\right|, \left|\frac{\Delta t_N^4\omega^4}{720}\right|, \left|\frac{\Delta t_N^4\omega^4}{360}\right|\right\} = \frac{\Delta t^4\omega^4}{360\times 2^{4m}} \le \varepsilon,\ \varepsilon = 10^{-16}. \tag{63}$$

From this, the critical value of m can be solved as

$$m_{\mathrm{cr}} = \frac{\log\left(\Delta t^4 \omega^4 / 360\varepsilon\right)}{4\log(2)}. \tag{64}$$

In the following, the performances of the AECM2 in dealing with rounding errors are discussed. The undamped case is firstly considered, in which $\xi = 0$, $\omega = \pi$, $x_0 = 1$, and $\dot{x}_0 = 1$. The absolute errors in displacement, velocity, and acceleration of the AECM2 and the Fox–Goodwin method are drawn in Figure 16, in which $\Delta t = 1$ and $\Delta t_N = 1/N$ are used in the AEC/DM2 and Fox–Goodwin method, respectively. The well-known Fox–Goodwin method is fourth-order accurate for the undamped system, whereas it is third-order accurate for the damped case. One can see from Figure 16 that the AECM2 and the Fox–Goodwin method have the same slope before $m < 13$, meaning that the AECM2 is strictly fourth-order accurate. Additionally, one can find that: (a) When $m > m_{\mathrm{cr}} = 13$, the absolute errors of the AECM2 trend to constants; (b) With the increase of m, the accuracy of the Fox–Goodwin method increases when $m < 13$, and then its accuracy begins to decline when $m \geq 13$.

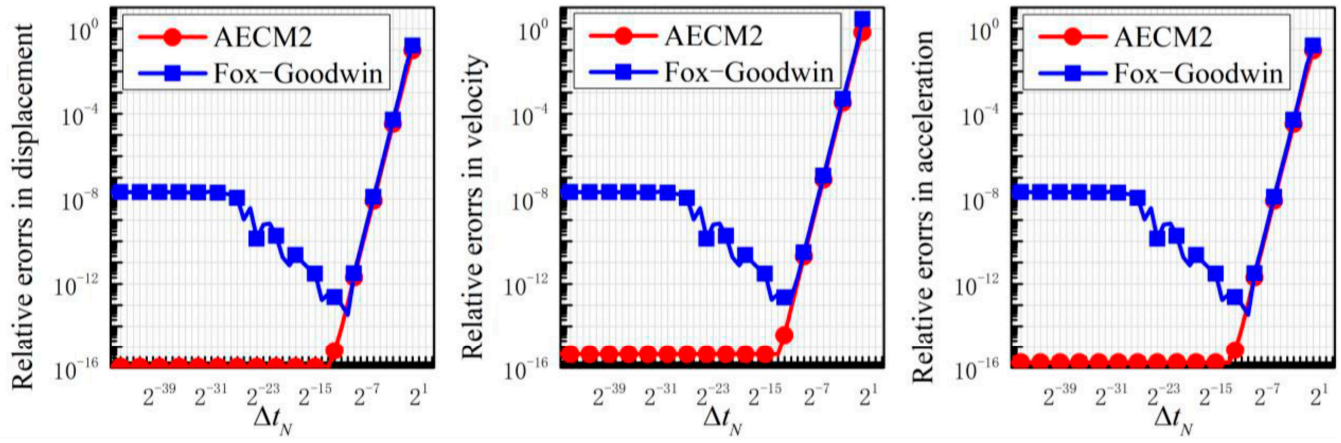

Figure 16. Relative errors in displacement, velocity, and acceleration of the AECM2 for the case of $\xi = 0$ and $f(t) = 0$.

Figure 17 plots the absolute errors of the two methods for the damped case, in which $\xi = 0.5$, $\omega = 2\pi$, $x_0 = 1$, and $\dot{x}_0 = 0$. One can see from Figure 17 that the AECM2 is fourth-order accurate, but the Fox–Goodwin method turns out to be third-order accurate due to the presence of physical damping. In addition, it follows that the accuracy of the AECM2 has no observable variation when $m > m_{\mathrm{cr}} = 13$; thus, m_{cr} given in Equation (64) is suitable for the analysis of damped dynamic systems. The critical values of m of the AECM2 are provided in Table 3, wherein one can find that compared with the second-order AECM1, the AECM2 has a smaller m_{cr} for the same $\omega\Delta t$. As shown in Figure 18, when $\omega\Delta t < 1$, the m_{cr} of the AECM2 is about 1/2~1/4 that of the AECM1, implying that the AECM2 enjoys an advantage in efficiency when applied to dynamic systems wherein the low-frequency modes dominate.

Table 3. The critical value of m of the AECM2 for different $\omega\Delta t$.

$\omega\Delta t$	0.01	0.1	1	10	20	50	100	1000	10,000
m_{cr}	5	8	12	15	16	17	18	22	25

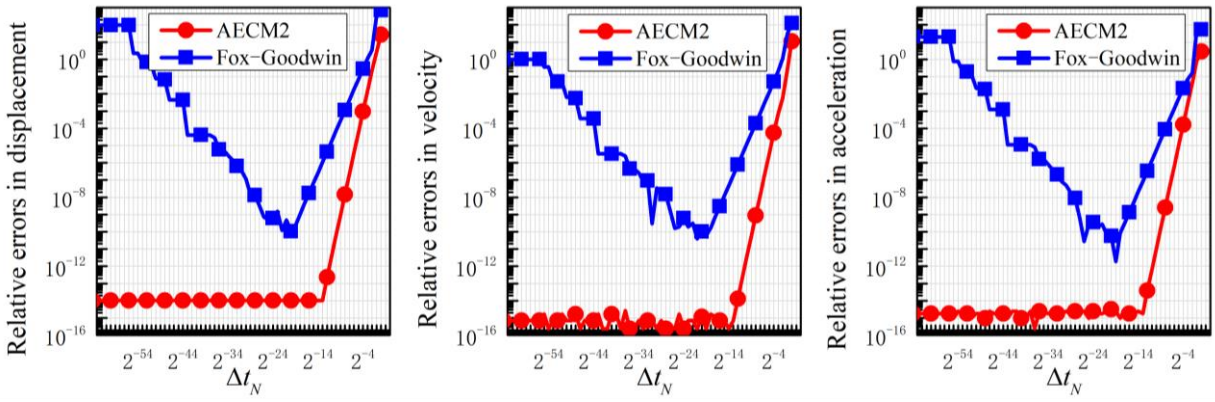

Figure 17. Relative errors in displacement, velocity, and acceleration of the AECM2 for the case of $\xi = 0.5$ and $f(t) = 0$.

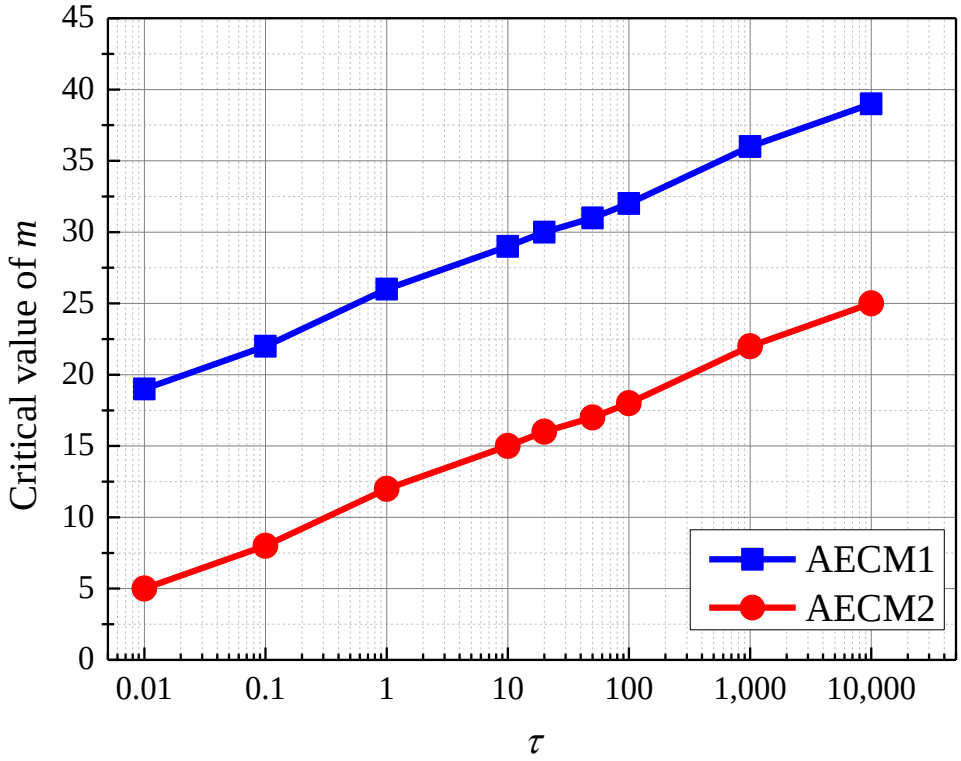

Figure 18. Critical values of m of the AECM1 and AECM2.

At last, the selection of the Gauss–Legendre nodes is discussed here. The standard SDOF test equation (35) is considered again, wherein $\xi = 2/\sqrt{5}$, $\omega = \sqrt{5}$, $x_0 = 57/65$, $\dot{x}_0 = 2/65$, and $f(t) = \sin(2t)$ are adopted. The absolute errors of the AECM2 and the Fox–Goodwin method are compared in Figure 19. It can be seen that: (a) The AECM2 is fourth-order accurate for the dynamic systems including external excitation; (b) Due to the rounding errors, the accuracy of the Fox–Goodwin method begins to decrease after $m > 24$; (c) The accuracy of the AECM2 trend to constants with the decrease in time-step size, and together with four Gauss–Legendre nodes, the accuracy of AECM2 is close to computer precision after $m > m_{cr} = 10$ is achieved from Equation (64). Then, four Gauss–Legendre nodes are employed in the AEC/DM2.

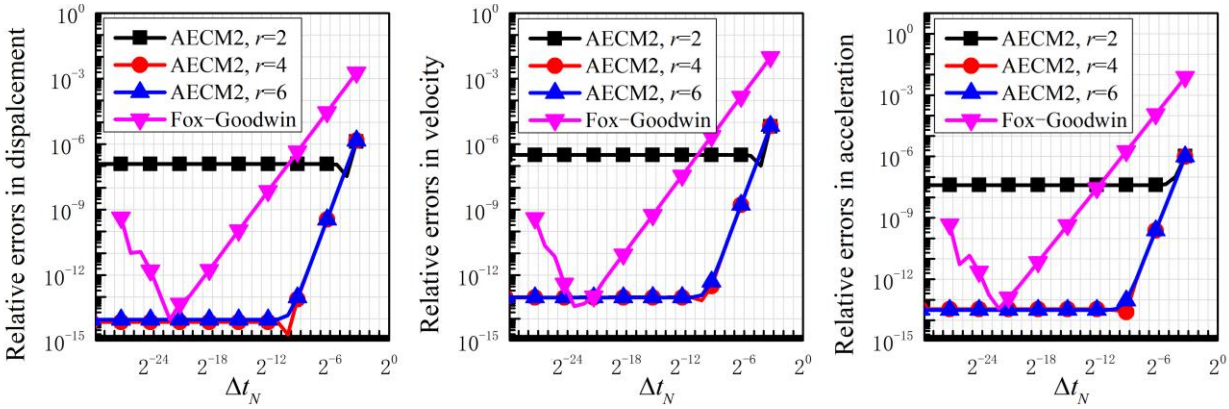

Figure 19. Relative errors in displacement, velocity, and acceleration of the AECM2 for the case of $\xi = 2/\sqrt{5}$ and $f(t) = \sin(2t)$ (r represents number of Gauss–Legendre nodes).

3.3. Overshoot Characteristics

The overshooting phenomenon may occur in the first several time steps. For a convergent method, there is no overshoot as $\tau \to 0$, so only the case of $\tau \to \infty$ needs to be considered. The analysis of overshooting should take into account the effect of physical damping. With physical damping, first-order overshooting components enter into several well-known time integration methods [53], which were previously thought to exhibit zero-order overshooting. The recursive schemes at the first step of the AEC/DM1 and AEC/DM2 are the same for the case of $\tau \to \infty$, which have the forms of

$$x_{t+\Delta t} \approx -\rho_\infty x_t \tag{65}$$

$$\text{and } \Delta t\dot{x}_{t+\Delta t} \approx \rho_\infty \Delta t\dot{x}_t. \tag{66}$$

Through the observation of Equations (65) and (66), one can find that the AEC/DM1 and AEC/DM2 are both zero-order overshoots. The SDOF system given in Equation (35) with $x_0 = 1$ and $\dot{x}_0 = 0$ is considered for testing overshooting behavior. Figures 20 and 21 draw the displacement and velocity of the AEC/DM1 and the AEC/DM2, respectively, at the first step versus $\Delta t/T$, and numerical results validate that our methods have no overshoots both in displacement and velocity.

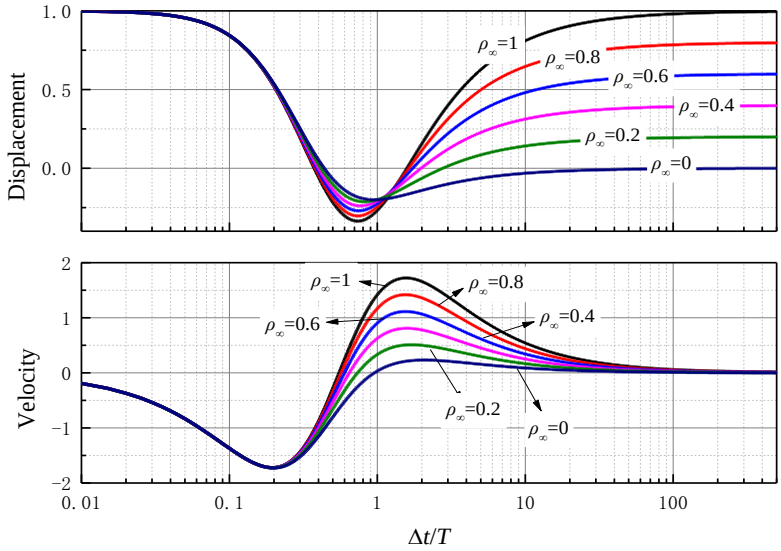

Figure 20. Displacement and velocity at the end of the first time step versus $\Delta t/T$ of the AEC/DM1.

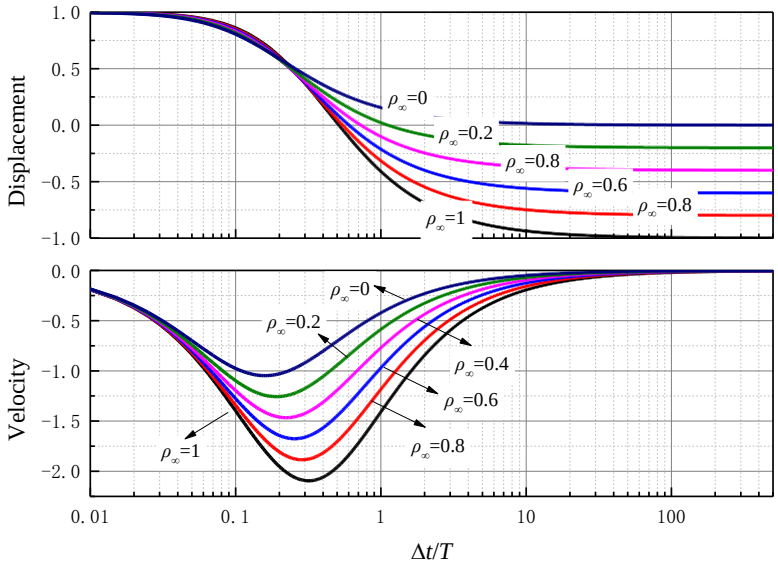

Figure 21. Displacement and velocity at the end of the first time step versus $\Delta t/T$ of the AEC/DM2.

4. Numerical Experiments

The theoretical analysis presented in Section 3 has shown that the time integrators, including the AEC/DM1 and the AEC/DM2 based on the proposed strategy, are unconditionally stable, controllably dissipative, higher-order accurate, and have zero-order overshoots. For linear systems, including the undamped and damped cases, the newly constructed time integrators can converge to computer precision with the increase of m. In this section, some representative linear and nonlinear dynamic systems are simulated to validate the advantages of the proposed methods in stability, accuracy, efficiency, and dissipation compared with some widely-used time integration methods.

4.1. Linear Systems

Two linear numerical experiments are conducted here to validate the conclusions given in Section 3, which can compare the accuracy and efficiency of the proposed methods and the well-known implicit methods, including the TR and Fox–Goodwin methods.

4.1.1. Stiff System

A subclass of the initial value problems [54] involving rapidly decaying transient solutions might arise in a wide variety of engineering applications, such as problems in chemical kinetics, the study of spring and damping systems, and the analysis of control systems. This type of problem is known as a stiff problem. Thus, to test the accuracy and efficiency of the proposed methods in dealing with stiff systems, the following mathematical model is considered as

$$\begin{bmatrix} \dot{y}_1 \\ \dot{y}_2 \end{bmatrix} = \begin{bmatrix} 0 & 1 \\ -10000 & -10001 \end{bmatrix} \begin{bmatrix} y_1 \\ y_2 \end{bmatrix}. \tag{67}$$

The initial conditions are taken to be $y_1(0) = 5$, $y_2(0) = -5$, and the theoretical solutions are

$$y_1(t) = 5\mathrm{e}^{-t}, y_2(t) = -5\mathrm{e}^{-t}. \tag{68}$$

From the governing equations, the natural frequency $\omega = 100$ and numerical damping ratio $\xi = 50.0050$. In this example, the time step sizes of these compared methods are assumed to be: Δt(AECM1) = 0.1, Δt(AECM2) = 0.2, Δt(TR) = 0.1, 0.01, and Δt(Fox–Goodwin) = 0.1, 0.01.

The results in y_1 of all methods are shown in Figure 22, in which one can find that: (a) Among these single-step methods, the higher-order accurate Fox–Goodwin method is unstable for the larger time step size $\Delta t = 0.1$ due to intrinsic conditional stability, while

other methods are convergent; (b) With the increase of m, the proposed methods' accuracy can be noticeably improved; (c) The AECM1 ($m > 25$) and AECM2 ($m > 15$) converge to computer precision 10^{-16}, validating that the m_{cr} given in Section 3 is reliable; (d) With the decrease of step size, the TR and Fox–Goodwin methods can both obtain higher accuracy, but their accuracy is far lower than that of the proposed methods.

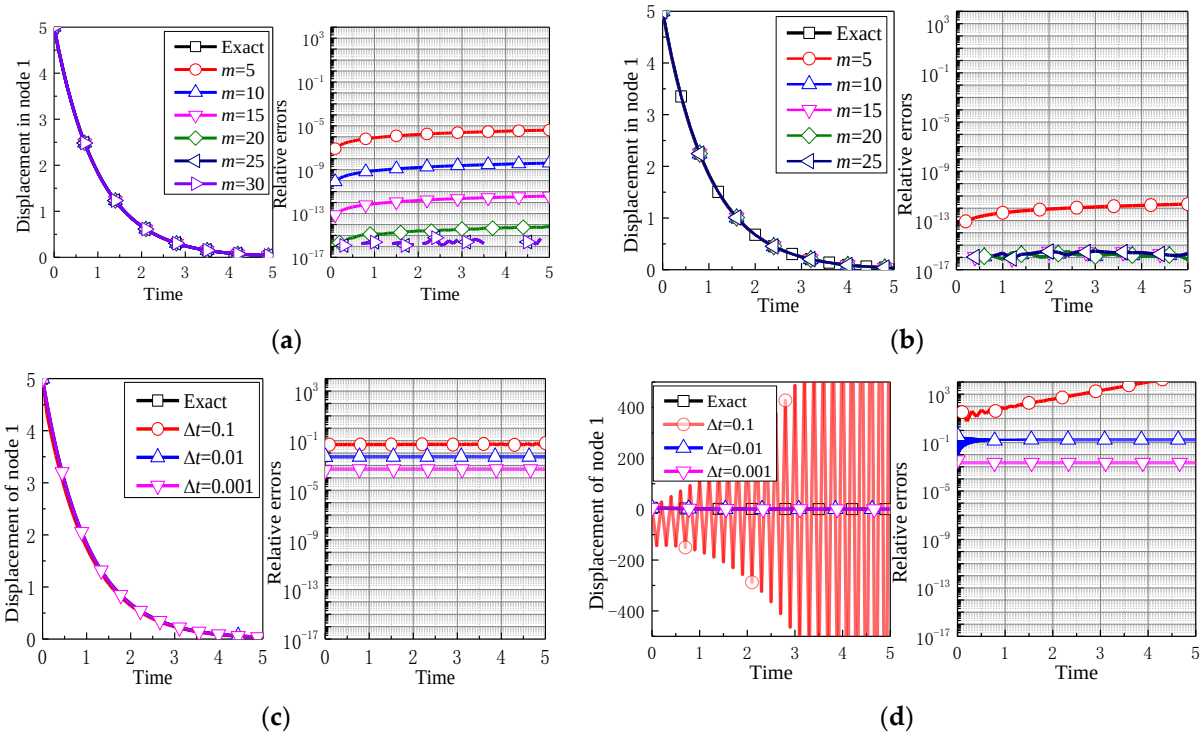

Figure 22. Displacement at the first node and absolute errors versus time: (**a**) AECM1; (**b**) AECM2; (**c**) TR; and (**d**) Fox–Goodwin.

The results in y_2 of these methods are drawn in Figure 23, and some new phenomena can be found. With physical damping, the first-order overshooting components enter into TR, meaning that they induce obvious oscillations for the larger time step size. Since the proposed methods have no overshoots both for undamped and damped systems, they can accurately simulate dynamic problems, including stiff modes.

Additionally, the CPUs of these methods are compared in Table 4. For the proposed methods, the CPU contains 'Preparations' and 'Recursions' in which 'Preparations' is the CPU time for the calculation of $\boldsymbol{A}_{\text{num}}(\Delta t\boldsymbol{H})$, and 'Recursions' represents recursive computations of all time steps. Considering that the DOFs of this example are only two, we only discuss the effect of the value of m and the size of the time step on computational costs. From Table 3, we can find that: (a) The value of m has little effect on the computations for the proposed methods, meaning that the proposed methods' can accuracy be enhanced without efficiency loss; (b) With the decrease of time step size, the accuracy of the TR and Fox–Goodwin methods can be slowly improved, and they need considerable computational costs.

It can be concluded from this example that: (a) Compared with the fourth-order Fox–Goodwin method with conditional stability, the higher-order accurate methods based on our strategy enjoy stability advantage; (b) The proposed methods can obtain computer precision without the extra cost of computations, but the methods based on the difference concept needs heavy burdens to obtain slightly accuracy improvement.

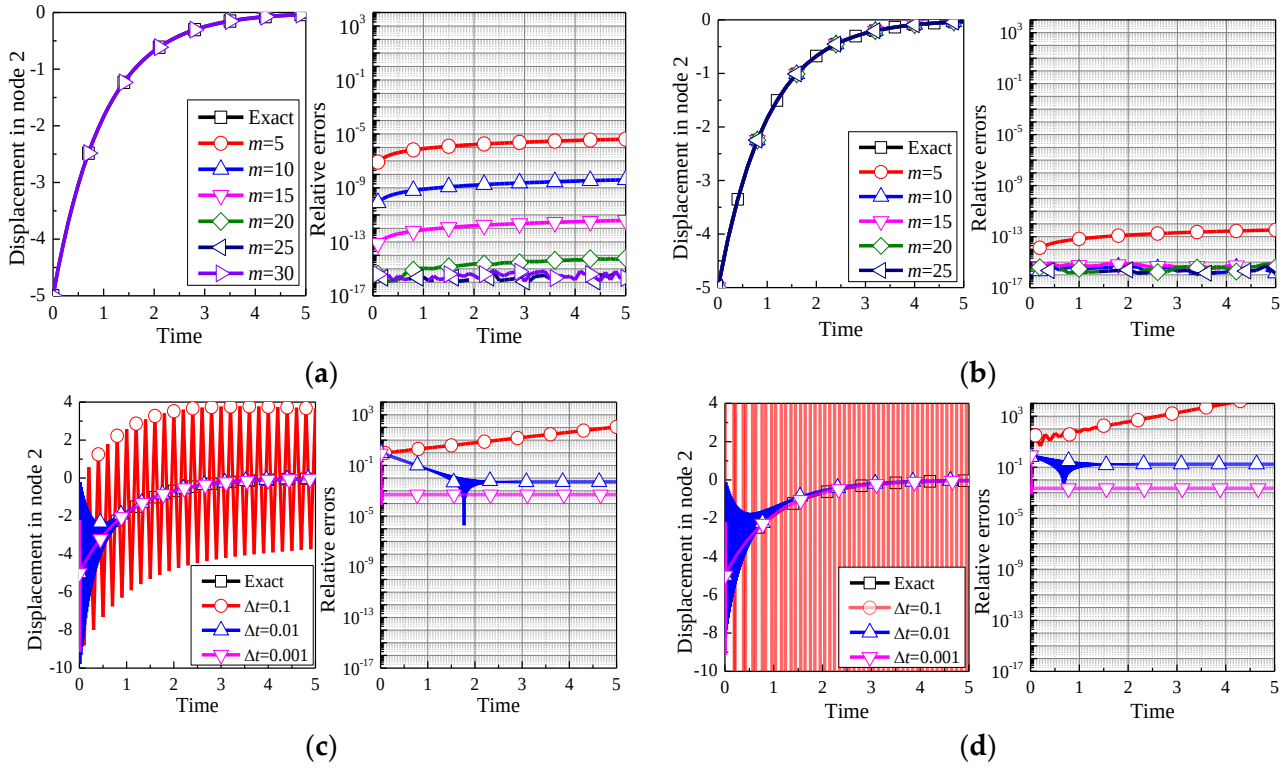

Figure 23. Displacement at the second node and absolute errors versus time: (**a**) AECM1; (**b**) AECM2; (**c**) TR; and (**d**) Fox–Goodwin.

Table 4. CPUs of the AECM1, AECM2, TR, and Fox–Goodwin in the interval [0, 500]s.

	AECM1				**AECM2**			
	***m* = 5**	***m* = 10**	***m* = 20**	***m* = 25**	***m* = 5**	***m* = 10**	***m* = 20**	***m* = 25**
Preparation	5.7800×10^{-5}	6.2700×10^{-5}	6.3500×10^{-5}	6.6700×10^{-5}	0.0016	0.0017	0.0018	0.0016
Recursion	0.0177	0.0135	0.0139	0.0138	0.0144	0.0125	0.0125	0.0109
Total	0.0178	0.0136	0.0140	0.0139	0.0160	0.0142	0.0143	0.0125
	TR				**Fox–Goodwin**			
	Δt = 0.1	**Δt = 0.01**	**Δt = 0.001**		**Δt = 0.1**	**Δt = 0.01**	**Δt = 0.001**	
Preparation	-	-	-		-	-	-	
Recursion	0.0100	0.1251	1.8498		0.0122	0.1063	1.3964	
Total	0.0100	0.1251	1.8498		0.0122	0.1063	1.3964	

4.1.2. Cantilever Plane Truss

The second example forces the accuracy and efficiency performance of the AECM1 and AECM2 in solving linear systems under external excitations. Figure 24 shows the material and geometry properties of the cantilever plane truss [55], which contains 25 repeated structures. In the vertical direction of nodes 42 and 52, two harmonic loads are applied, which have the forms of

$$f_1(t) = -2\sin(1000t)\text{MN} \tag{69}$$

$$\text{and } f_2(t) = -2\sin(10000t)\text{MN}. \tag{70}$$

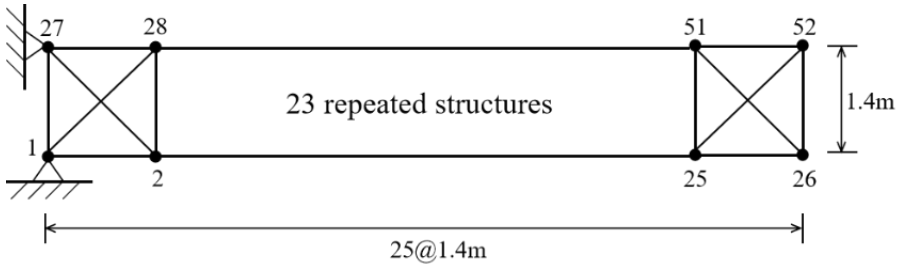

Figure 24. Cantilever plane truss.

The structure has 52 nodes, 226 elements, and 100 DOFs. The modulus of elasticity, density, and sectional areas are $E = 2.5 \times 10^{11}$ N/m^2, $\rho = 1.78 \times 10^3$ kg/m^3, and $A = 1.96 \times 10^{-3}$ m^2, respectively. In this example, $\Delta t = 10^{-5}$ is used in the proposed methods, and $\Delta t = 10^{-5}$, $\Delta t = 10^{-6}$, and $\Delta t = 10^{-7}$ are employed in the TR and Fox–Goodwin methods. The maximum natural frequency of the cantilever plane truss is 24,378, and then the m_{cr} for the AECM1 and the AECM2 can be determined from Section 3, which are 22 and 8, respectively.

The numerical results of these methods are compared in Figures 25–27, from which one can conclude that: (a) The accuracy of the AECM1 no longer improves after $m > 20$, and if $m > 5$, the accuracy of the AECM2 is the same, validating that the reliability of theoretical analysis about m_{cr}; (b) The accuracy improvement of the proposed methods can be achieved by increasing m, while other methods can increase accuracy by decreasing the step size; (c) Among them, the second-order accuracy TR exhibits observable numerical errors in the simulations of velocities and accelerations.

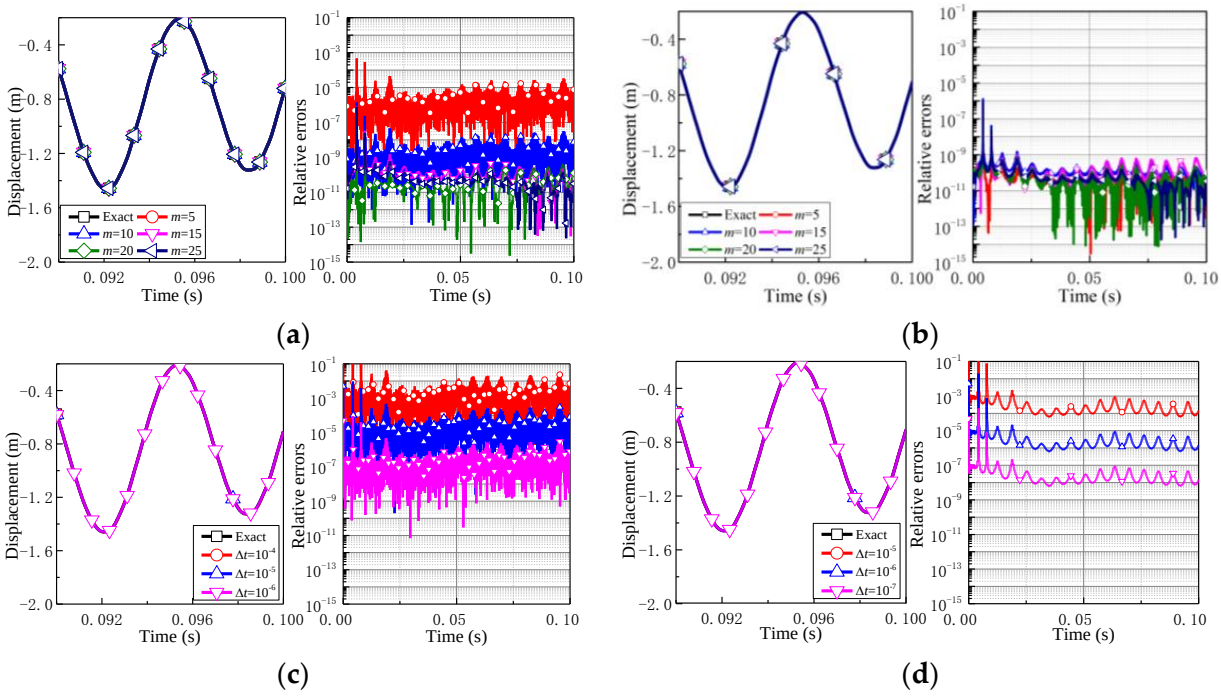

Figure 25. Displacement of node 52 in vertical direction and absolute errors: (**a**) AECM1; (**b**) AECM2; (**c**) TR; and (**d**) Fox–Goodwin.

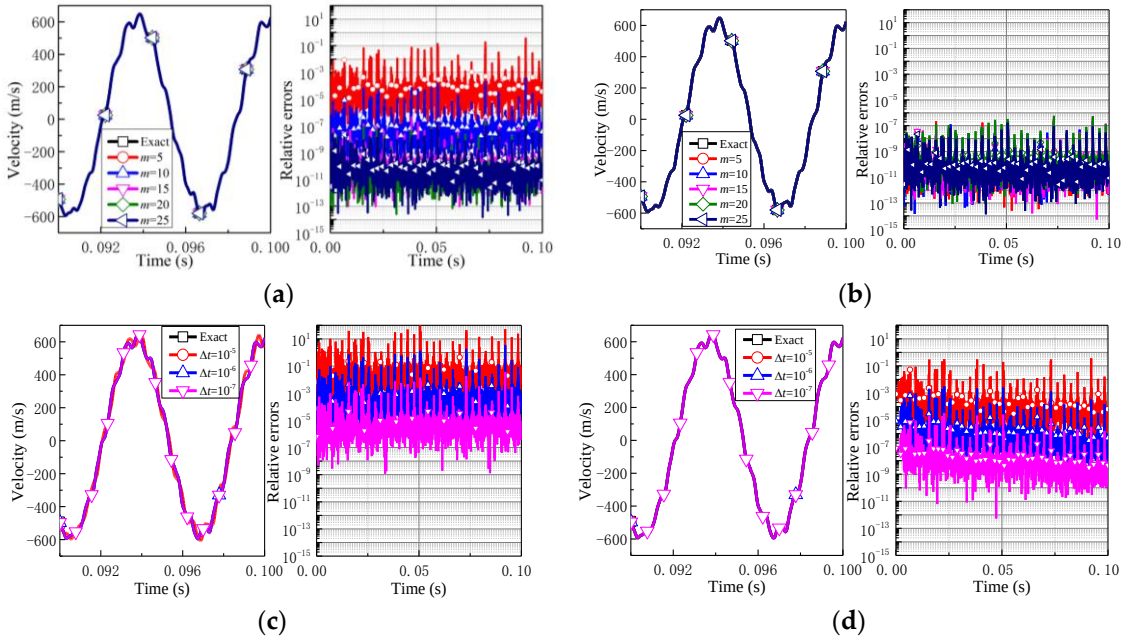

Figure 26. Velocity of node 52 in a vertical direction and absolute errors: (**a**) AECM1; (**b**) AECM2; (**c**) TR; and (**d**) Fox–Goodwin.

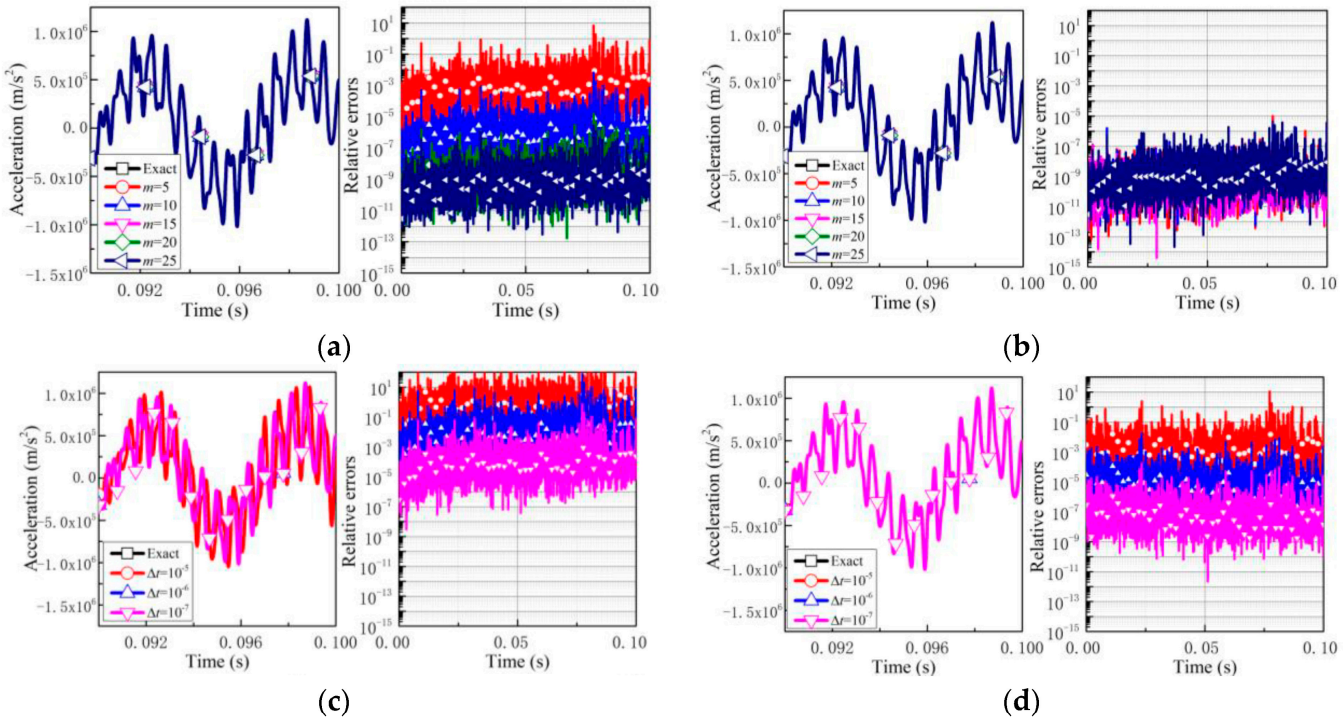

Figure 27. Acceleration of node 52 in a vertical direction and absolute errors: (**a**) AECM1; (**b**) AECM2; (**c**) TR; and (**d**) Fox–Goodwin.

Additionally, the CPUs of these methods are compared in Table 5. It can be seen that: (a) With the increase of m, the proposed methods almost do not produce extra computations; (b) The computational efficiency of the TR and Fox–Goodwin methods dramatically drop with the decrease of the time step size; (c) The TR and Fox–Goodwin methods with $\Delta t = 10^{-6}$ have the same costs with those of the proposed methods, but our methods perform with higher accuracy.

Table 5. CPUs of the AECM1, AECM2, TR, and Fox–Goodwin in the interval [0, 0.1]s.

	AECM1				**AECM2**			
	$m = 5$	$m = 10$	$m = 20$	$m = 25$	$m = 5$	$m = 10$	$m = 20$	$m = 25$
Preparation	0.0183	0.0254	0.0353	0.0385	0.0209	0.0286	0.0383	0.0459
Recursion	2.2373	2.4461	2.8605	2.8807	2.7853	2.6430	2.9451	2.9320
Total	2.2556	2.4715	2.8958	2.9192	2.8062	2.6716	2.9834	2.9779
	TR				**Fox–Goodwin**			
	$\Delta t = 10^{-5}$	$\Delta t = 10^{-6}$	$\Delta t = 10^{-7}$		$\Delta t = 10^{-5}$	$\Delta t = 10^{-6}$	$\Delta t = 10^{-7}$	
Preparation	-	-	-		-	-	-	
Recursion	0.1629	1.8562	26.8233		0.1306	1.8313	21.9914	
Total	0.1629	1.8562	26.8233		0.1306	1.8313	21.9914	

4.2. Nonlinear Systems

Some representative nonlinear numerical examples are considered in this section. As applied to nonlinear dynamic systems, the proposed methods do not need the Newton iteration method; thus, they are compared with some well-known explicit methods, including the second-order modified Euler method and the classical fourth-order Runge–Kutta method (noted as RK4). Additionally, some advanced multi-step methods and composite methods are considered for comparison.

4.2.1. Averaged System in Wind-Induced Oscillation

The first nonlinear example considers an average system [43] in wind-induced oscillation, and its motion of equation has the form of

$$\begin{cases} \dot{x}_1 = -\zeta x_1 - \lambda x_2 + x_1 x_2 \\ \dot{x}_2 = \lambda x_1 - \zeta x_2 + 0.5\left(x_1^2 - x_2^2\right) \end{cases}, \tag{71}$$

where $\zeta \geq 0$ is a damping factor and λ is a detuning parameter with $\zeta = r\cos(\theta)$, $\lambda = r\sin(\theta)$, and $\zeta \geq 0$, $0 \leq \theta \leq \pi/2$. The case of $\theta = \pi/2$ is considered here to analyze the energy-conservation ability of the proposed methods, and the corresponding energy function of this system is

$$E = 0.5r\left(x_1^2 + x_2^2\right) - 0.5\sin\theta\left(x_1^2 x_2 - 1/3x_2^3\right) + 0.5\cos\theta\left(1/3x_2^3 - x_1^2 x_2\right). \tag{72}$$

Consider the initial conditions $x_1(0) = 0$ and $x_2(0) = 1$, and $r = 200$. To improve the stability of these proposed methods in solving dynamic systems, including geometric nonlinearity, $\rho_\infty = 0$ is utilized. The AEDM1 and AEDM2 adopt $\Delta t = 1/(2r)$ and $\Delta t = 1/r$, respectively; $\Delta t = 1/(8r)$, $\Delta t = 1/(15r)$ and $\Delta t = 1/(20r)$ are used in the modified Euler method; $\Delta t = 1/(4r)$, $\Delta t = 1/(10r)$ and $\Delta t = 1/(15r)$ are used in the RK4 method. The relative values of energy errors of these methods are plotted in Figure 28, and Table 6 provides their computations. One can find that: (a) With the increase of the m, the accuracy of the AEDM1 and AEDM2 can be obviously enhanced without additional burdens; (b) The accuracy of the modified Euler method and the RK4 method can be improved by decreasing the size of time step; (c) When the computations of these methods are the roughly same, the AEDM2 is four orders of magnitude more accurate than the modified Euler method and the RK method.

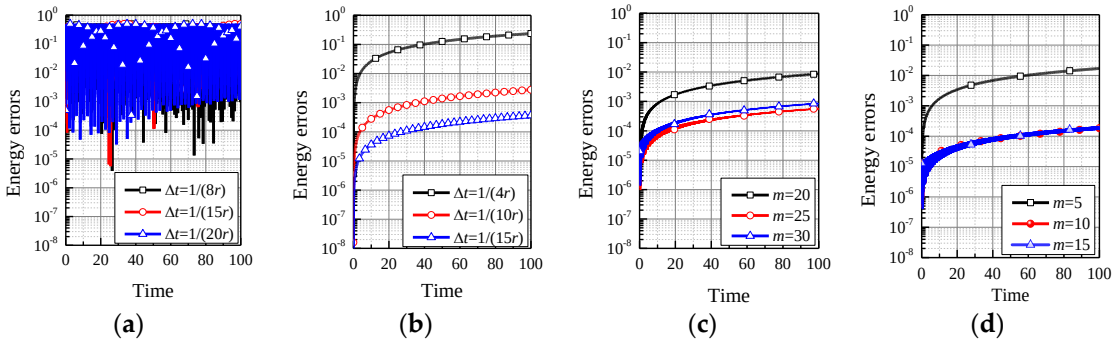

Figure 28. Energy errors of these methods versus time: (**a**) Euler; (**b**) RK4; (**c**) AEDM1; and (**d**) AEDM2.

Table 6. CPUs of the AEDM1, AEDM2, Euler, and RK4 in the simulations of the interval [0, 1000]s.

	AEDM1			**AEDM2**		
	***m* = 20**	***m* = 25**	***m* = 30**	***m* = 5**	***m* = 10**	***m* = 15**
Preparation	0.000169	0.000140	0.000396	0.002044	0.001902	0.002686
Recursion	4.006249	4.395022	4.950563	4.867872	5.423115	6.616388
Total	4.006418	4.395162	4.950959	4.869916	5.425017	6.619074
	Euler			**RK4**		
	Δt = 1/(8*r*)	**Δt = 1/(15 *r*)**	**Δt = 1/(20 *r*)**	**Δt = 1/(4 *r*)**	**Δt = 1/(10 *r*)**	**Δt = 1/(15 *r*)**
Preparation	-	-	-	-	-	-
Recursion	4.054805	6.3309	10.699817	7.299833	16.232617	26.404818
Total	4.054805	6.3309	10.699817	7.299833	16.232617	26.404818

In terms of the initial conditions, we can find the suggested m of the proposed methods as when applied to nonlinear systems. From Equation (71), one can read that the Jacobin matrix of this system at the initial moment has the form of

$$\boldsymbol{J} = \begin{bmatrix} -\zeta + x_2(0) & -\lambda \\ \lambda + x_1(0) & -\zeta - x_2(0) \end{bmatrix} = \begin{bmatrix} 1 & -200 \\ 200 & -1 \end{bmatrix}. \tag{73}$$

Then, the norms of two eigenvalues can be solved, which are equal to 199.9975. In this example, if the time step sizes of the AEDM1 and AEDM2 are 0.0025 and 0.005, respectively, then the $\omega\Delta t$ of them are 0.5 and 1, respectively. Therefore, the m_{cr} can be obtained from Tables 2 and 3, and m_{cr} = 22~26 for AEDM1 and m_{cr} = 12 for AEDM2. From Figure 28, one can observe that the AEDM1 with $m > 25$ and the AEDM2 with $m > 10$ have no observable accuracy improvements. In a way, as applied to nonlinear systems, the proposed methods can select appropriate values of m in terms of the initial dynamic characteristic of nonlinear problems.

4.2.2. Seven-Story Shear Building with Bouc–Wen Hysteresis Model

For analyzing the accuracy and efficiency of the AECMn in solving nonlinear systems with physical damping, the second nonlinear example considers a seven-story shear building containing the Bouc–Wen hysteresis model [56–58]. The system is idealized as a simple shear model with seven DOFs, as shown in Figure 29, and it is subjected to sinusoidal excitation.

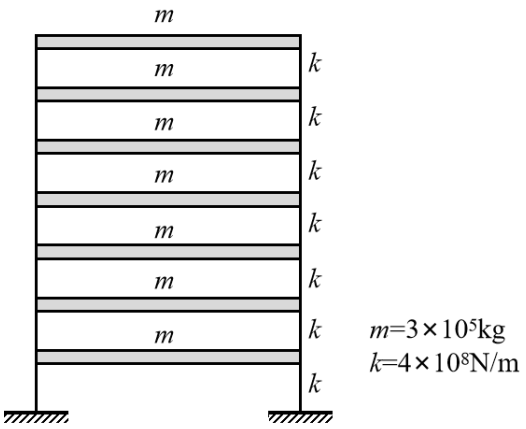

Figure 29. Seven-story shear building.

The governing equation of the system with viscous damping and a hysteretic restoring force given by the Bouc–Wen hysteresis model has the form of

$$\boldsymbol{M}\ddot{\boldsymbol{x}} + \boldsymbol{C}\dot{\boldsymbol{x}} + \mu\boldsymbol{K}\boldsymbol{x} + (1-\mu)\boldsymbol{K}\boldsymbol{z} = -\boldsymbol{M}\ddot{\boldsymbol{x}}_g, \tag{74}$$

where μ is the rigidity ratio that separates the restoring force into a linear component and a hysteretic component; $\boldsymbol{z}$ represents the hysteretic displacement vector related to the displacement $\boldsymbol{x}$; $\ddot{\boldsymbol{x}}_g$ is the vector of ground motion acceleration which has the form of $\ddot{\boldsymbol{x}}_g = [\boldsymbol{0}^{\mathrm{T}}\ \sin(t)]^{\mathrm{T}}$. In this model, the damping matrix $\boldsymbol{C}$ is defined as

$$\boldsymbol{C} = \alpha\boldsymbol{M} + \beta\boldsymbol{K},\ \alpha = 2\frac{\xi_1\omega_1\omega_2^2 - \xi_2\omega_2\omega_1^2}{\omega_2^2 - \omega_1^2},\ \beta = 2\frac{\xi_2\omega_2 - \xi_1\omega_1}{\omega_2^2 - \omega_1^2}, \tag{75}$$

where ξ_1 and ξ_2 are the viscous damping ratios, which are assumed to be 3% and 5%, respectively, and ω_1 and ω_2 are the first two frequencies. The hysteretic displacement vector $\boldsymbol{z}$ is formulated as

$$\dot{z}_l(t) = h(z_l)\frac{A\dot{x}_l(t) - v_z(t)\left(\beta_z\left|\dot{x}_l(t)\right||z_l(t)|^{n_z-1}z_l(t) + \gamma_z\dot{x}_l(t)|z_l(t)|^{n_z}\right)}{\eta_z(t)}, \tag{76}$$

where l is the number of elements; A determines the tangent stiffness; β_z, $\gamma_{z,}$ and n_z stand for the hysteretic shape parameters; $h(z_l)$ stands for the pinching function; $v_z(t)$ and $\eta_z(t)$ are the strength and stiffness degradation functions, respectively. The $v_z(t)$ and $\eta_z(t)$ can be obtained by setting

$$v_z(t) = 1 + \delta_v\varepsilon(t),\ \eta_z(t) = 1 + \delta_\eta\varepsilon(t), \tag{77}$$

where δ_v and δ_η represent the strength and stiffness degradation ratios, respectively; the hysteretic energy function $\varepsilon(t)$ has the form of

$$\varepsilon(t) = \int_0^t f_{z,l}(t)\dot{x}(t)\mathrm{d}t, \tag{78}$$

where $f_{z,l}(t)$ represents the associated internal hysteretic force variables collected in the hysteretic restoring force vector (1-μ)$\boldsymbol{K}\boldsymbol{z}(t)$. The pinching function $h(z_l)$ is formulated as

$$h(z_l) = 1 - \zeta_1(t)\exp\left(-\left(z_l(t)\mathrm{sgn}\left(\dot{x}_l(t)\right) - q_z z_{u,l}\right)^2/\zeta_2^2(t)\right), \tag{79}$$

where sgn(.) is the signum function; q_z represents a constant that sets the pinching level as a fraction of $z_{\max}$; $z_{u,l}$ is the ultimate value of $z_l(t)$, which is obtained by

$$z_{u,l} = \left(\frac{1}{v_z(\beta_z + \gamma_z)}\right)^{1/n_z}. \tag{80}$$

The ζ_1(t) controls the magnitude of the initial drop in slope, which is given by

$$\zeta_1(t) = \zeta_s(1 - \exp(-p_z\varepsilon(t))), \tag{81}$$

where p_z is a constant that contributes to the rate of the initial drop in slope and ζ_s is the measure of total slip. The ζ_2(t) causes the pinching region to spread, and its expression is

$$\zeta_2(t) = (\psi + \delta_\psi)(\lambda + \zeta_1(t)), \tag{82}$$

where ψ and δ_ψ represent the pinching magnitude and rate, respectively; λ is a parameter that controls the variation rate of ζ_2(t) with a change of ζ_1(t). The hysteretic model is controlled by the above-mentioned 13 parameters, which are $\{A, \mu, \beta_z, \gamma_z, n_z, \delta_v, \delta_\eta, \zeta_s, p_z, q_z, \psi, \delta_\psi, \lambda\}$ wherein $\{\mu, \beta_z, \gamma_z, n_z\}$ determine the shape of the hysteretic model; $\{\delta_v, \delta_\eta\}$ control the system degradation; $\{\zeta_s, p_z, q_z, \psi, \delta_\psi, \lambda\}$ control the pinching phenomenon. In this example, these parameters are assumed to be $A = 1$, $\mu = 0.02$, $\beta_z = 100$, $\gamma_z = 100$, $n_z = 1.1$, $\delta_v = 0.02$, $\delta_\eta = 0.1$, $p_z = 0.02$, $q_z = 0.3$, $\zeta_s = 0.9$, $\psi = 0.1$, $\delta_\psi = 0.11$, and $\lambda = 0.1$.

The displacement and velocity of the bottom story are shown in Figures 30–33, in which the AECM1 and AECM2 adopt $\Delta t = 0.004$ and $\Delta t = 0.008$, respectively; $\Delta t = 0.001$, $\Delta t = 0.0002$, and $\Delta t = 0.0001$ are used in the modified Euler method; $\Delta t = 0.002$, $\Delta t = 0.0004$, and $\Delta t = 0.0002$ are used in the RK4 method. The reference solution is obtained by the AECM2 with $m = 20$ using a smaller time step size. The CPUs of these methods are provided in Table 7. It can be found that: (a) With the decrease of time step size, both the modified Euler method and the RK4 method are closer to the reference solution, and the accuracy of the proposed methods can be enhanced by increasing m; (b) Under the same computations, the accuracy of the proposed methods is far higher than that of other methods. To further compare the accuracy of the AECM1 and AECM2, Figure 34 plots their relative errors in displacement, wherein one can see that the accuracy of the AECM2 is higher than that of the AECM1.

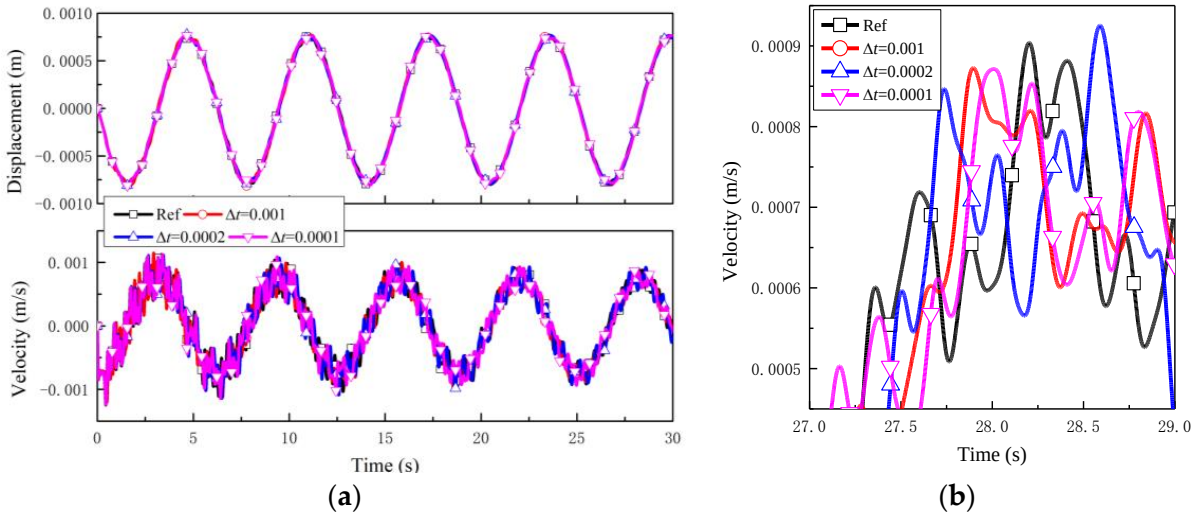

(**a**) (**b**)

Figure 30. Numerical results of the modified Euler method at the bottom story: (**a**) Numerical results of the bottom story in the [0, 30]s; (**b**) Velocity of the bottom story in the [27, 29]s.

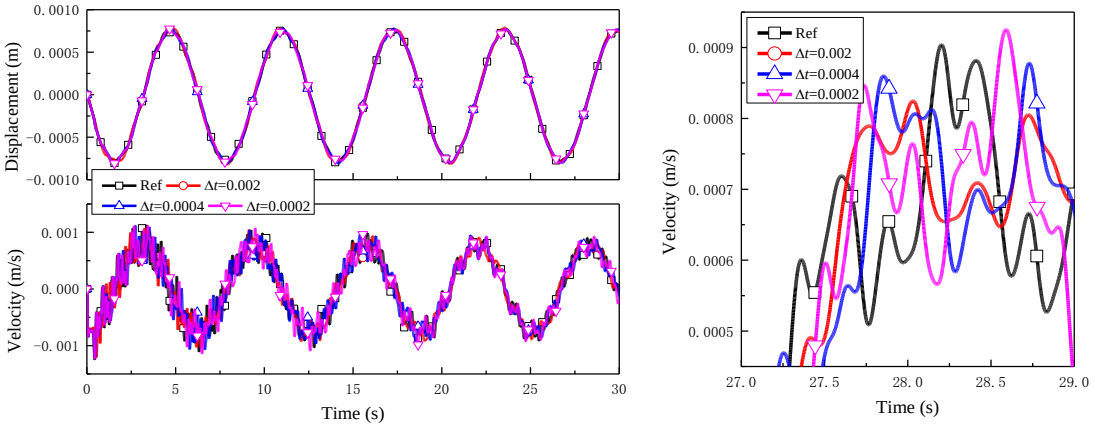

Figure 31. Numerical results of the RK4 method at the bottom story: (**a**) Numerical results of the bottom story in the [0, 30]s; (**b**) Velocity of the bottom story in the [27, 29]s.

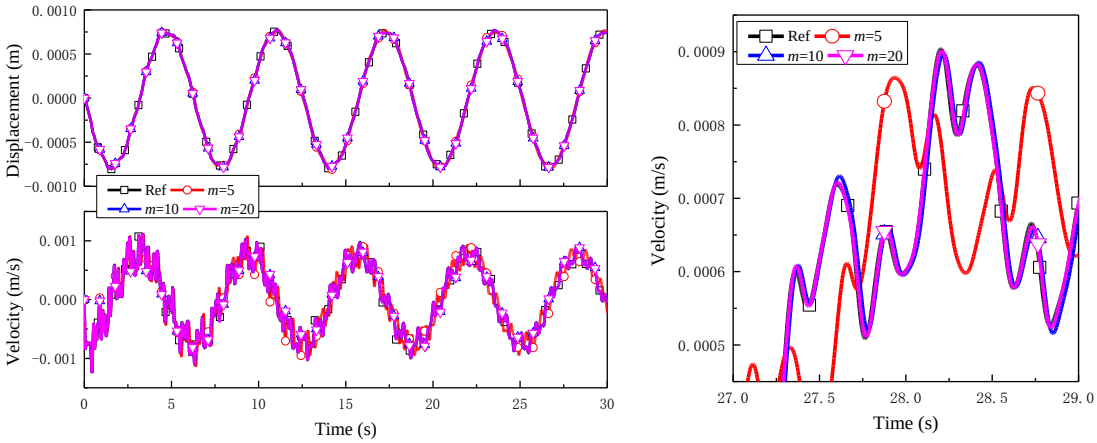

Figure 32. Numerical results of the AECM1 at the bottom story: (**a**) Numerical results of the bottom story in the [0, 30]s; (**b**) Velocity of the bottom story in the [27, 29]s.

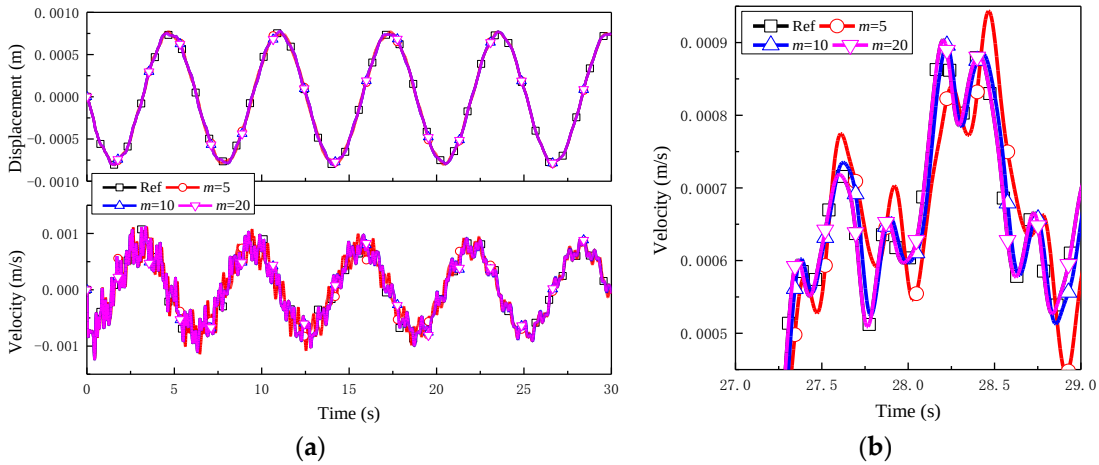

Figure 33. Numerical results of the AECM2 at the bottom story: (**a**) Numerical results of the bottom story in the [0, 30]s; (**b**) Velocity of the bottom story in the [27, 29]s.

Table 7. CPUs of the AECM1, AECM2, Euler, and RK4 in the simulations of the interval [0, 30]s.

	AECM1			**AECM2**		
	m **= 5**	m **= 10**	m **= 20**	m **= 5**	m **= 10**	m **= 20**
Preparation	7.2980×10^{-4}	5.4800×10^{-4}	7.3120×10^{-4}	0.0027	0.0029	0.0029
Recursion	25.7393	26.2247	27.3551	23.0725	23.5911	25.9989
Total	25.7400	26.2252	27.3558	23.0752	23.5940	26.0018
	Euler			**RK4**		
	Δt **= 0.001**	Δt **= 0.0002**	Δt **= 0.0001**	Δt **= 0.002**	Δt **= 0.0004**	Δt **= 0.0002**
Preparation	-	-	-	-	-	-
Recursion	16.3542	75.2145	155.6917	14.6172	58.4983	139.2688
Total	16.3542	75.2145	155.6917	14.6172	58.4983	139.2688

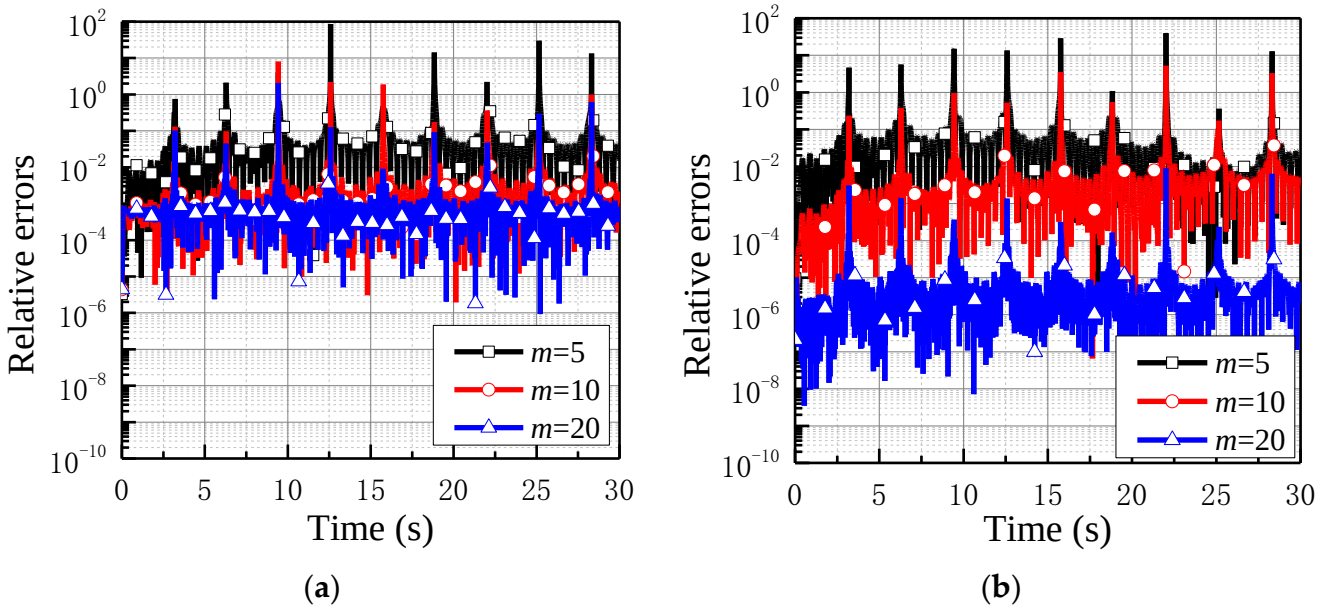

Figure 34. Relative errors of the AECM1 and AECM2 in displacement at the bottom story: (**a**) AECM1; and (**b**) AECM2.

4.2.3. N-Degree-of-Freedom Mass-Spring System

The last example considers an N-degree-of-freedom mass-spring system [59], as shown in Figure 35, to investigate the efficiency performances of the proposed methods in solving large-scale nonlinear problems. The system parameters are as follows:

$$m_i = 1 \quad i = 1, \ldots, N \tag{83}$$

$$\text{and } k_i = \begin{cases} k & i = 1 \\ k\left[1 + \alpha(x_i - x_{i-1})^2\right] & 2 \le i \le N' \end{cases} \tag{84}$$

where $k = 10^5$ N/m and $\alpha = -2$. Additionally, all masses are subjected to the external forces of $f_i(\mathrm{t}) = m_i \sin(t)$ $(i = 1, \ldots, N)$. In this example, two advanced time integration methods, the LMS2 [60] and the ρ_∞-Bathe method [10], are considered for comparison. The two-step LMS2 is especially effective for stiff systems, and the two-sub-step ρ_∞-Bathe method has been integrated with ADINA due to its superior properties. With zero initial conditions, two cases of $N = 100$ and 1000 are simulated.

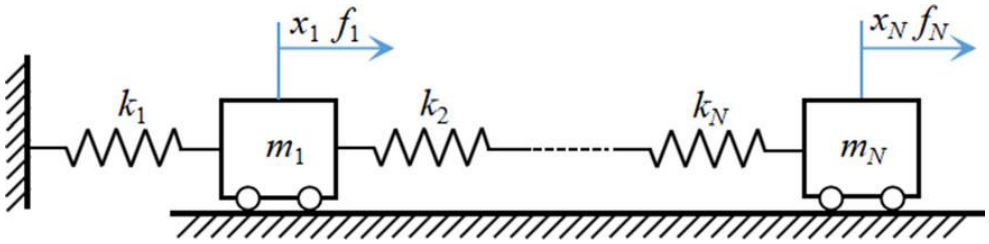

Figure 35. Mass-spring system.

The results of the AECM1 (m = 3, Δt = 0.01 s), the AECM2 (m = 3, Δt = 0.015 s), the LMS2 (Δt = 0.001 s), and the ρ_∞-Bathe method (Δt = 0.002 s) are drawn in Figures 36 and 37, and their computations are provided in Tables 8 and 9. It can be concluded that under the same accuracy performances and compared with the LMS2 and the ρ_∞-Bathe method, the AECM1 and the AECM2 perform considerable advantages in computational efficiency, especially for dynamic problems containing large degree-of-freedoms.

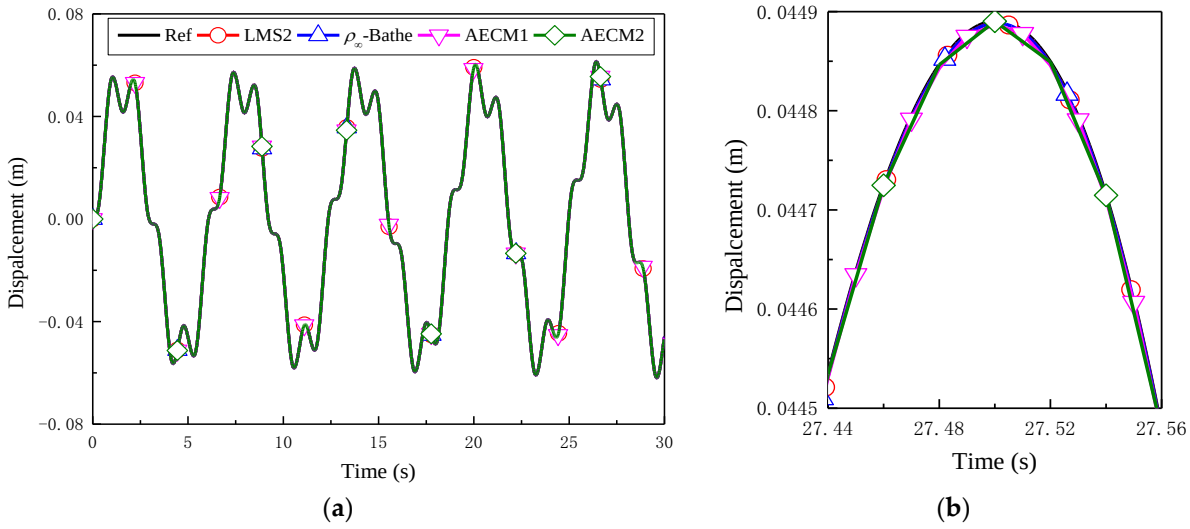

(**a**) (**b**)

Figure 36. Displacement of the Nth mass (N = 100): (**a**) Simulations in the interval [0, 30]s; (**b**) Simulations in the interval [27.44, 27.56]s.

Table 8. CPUs of the AECM1, AECM2, LMS2, and ρ_∞-Bathe method (N = 100, Total = 30 s).

	AECM1	**AECM2**	**LMS2**	**ρ_∞-Bathe**
Preparation	0.0197	0.0184	-	-
Recursion	3.7715	2.4026	19.8547	19.5784
Total	3.7912	2.4210	19.8547	19.5784

Table 9. CPUs of the AECM1, AECM2, LMS2, and ρ_∞-Bathe method (N = 1000, Total = 30 s).

	AECM1	**AECM2**	**LMS2**	**ρ_∞-Bathe**
Preparation	13.6961	22.8801	-	-
Recursion	339.4413	248.7944	820.9083	686.0195
Total	353.1374	271.6745	820.9083	686.0195

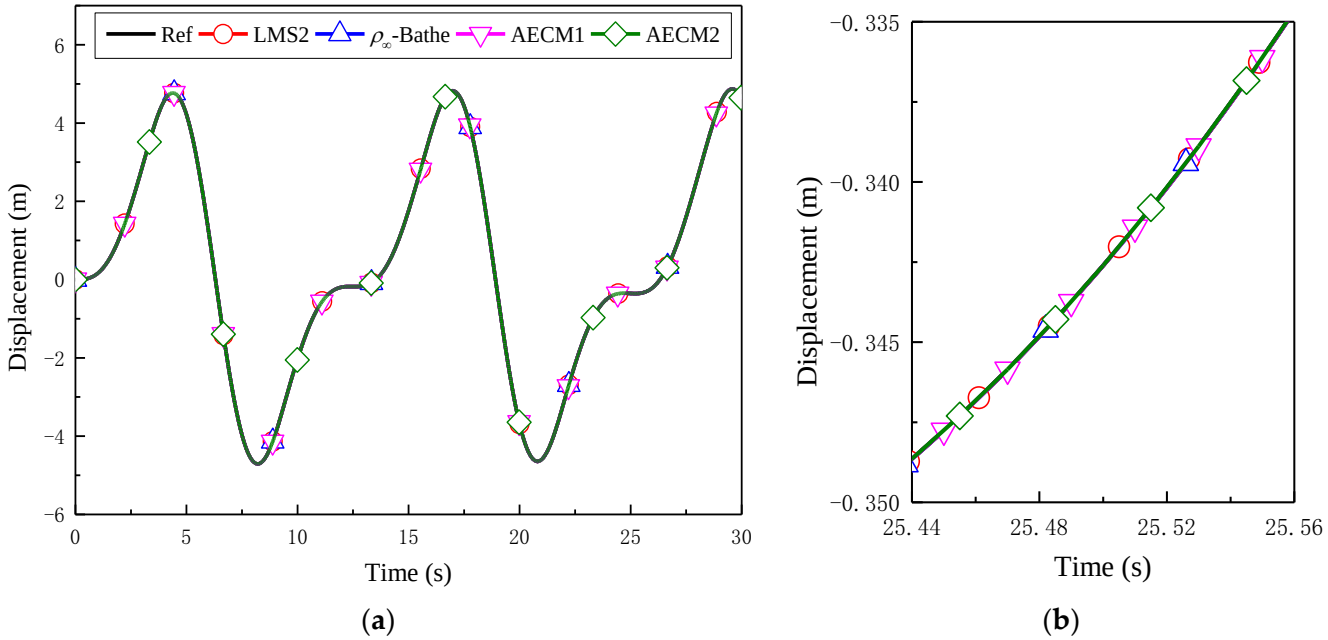

Figure 37. Displacement of the Nth mass (N = 1000): (**a**) Simulations in the interval [0, 30]s; (**b**) Simulations in the interval [25.44, 25.56]s.

5. Conclusions

For the analysis of dynamic systems, this work proposed a family of highly accurate and efficient time integration methods, named the AEC/DMn, based on the generalized Padé approximation, Gauss–Legendre quadrature, and explicit Runge–Kutta method, which was used to calculate function values at Gauss–Legendre quadrature points. The proposed methods can achieve higher-order accuracy, controllable dissipation, and unconditional stability. The 2^m algorithm and the storage of an incremental matrix method were adopted in the proposed methods to quickly and accurately transfer the response of the linear responses, and the nonlinear responses are approximated by the Gauss–Legendre quadrature and explicit Runge–Kutta method. For linear-free vibration problems, the proposed methods can converge to computer precision, and for linear-forced vibration problems and nonlinear problems, the proposed methods enjoy considerable advantages both in accuracy and efficiency compared with the widely-used time integration methods.

The second-order method (AEC/DM1) and the fourth-order method (AEC/DM2) were deeply studied. Their numerical properties, including the spectral characteristics, the rounding errors, and the overshoot characteristics, are deliberately investigated. Additionally, through the analysis of rounding errors, the critical values of sub-steps m that make numerical results converge to computer precision were found. Numerical experiments validated that the two methods have obvious accuracy and efficiency advantages compared with some widely-used methods, and the critical values of m given in this work are reliable. It was concluded from the theoretical analysis and numerical experiments that the speed of the fourth-order AEC/DM2 in accuracy improvement is quicker than that of the second-order AEC/DM1. In a way, this work has provided good candidates for the analysis of transient problems that widely exist in structural dynamics, multibody dynamics, heat conduction, and so on.

Author Contributions: Conceptualization, Y.J.; data curation, Y.J.; funding acquisition, Y.J. and Y.X.; software, Y.J.; supervision, Y.X.; validation, Y.J.; writing—original draft, Y.J.; writing—review and editing, Y.X. All authors have read and agreed to the published version of the manuscript.

Funding: This work was supported by the National Natural Science Foundation of China (12202058, 12172023, and 11872090), the China Postdoctoral Science Foundation (2022M710386), and the Outstanding Research Project of Shen Yuan Honors College BUAA (230121104).

Data Availability Statement: Not applicable.

Conflicts of Interest: The authors declare that they have no conflict of interest.

References

1. Hughes, T.J.R. *The Finite Element Method: Linear Static and Dynamic Finite Element Analysis*; Prentice-Hall: Englewood Cliffs, NJ, USA, 1987.
2. Saleh, M.; Kovacs, E.; Barna, I.F.; Matyas, L. New analytical results and comparison of 14 numerical schemes for the diffusion equation with space-dependent diffusion coefficient. *Mathematics* **2022**, *10*, 2813. [CrossRef]
3. Butcher, J.C. *Numerical Methods for Ordinary Differential Equations*; John Wiley & Sons, Ltd.: Chichester, UK, 2016.
4. Bank, R.E.; Coughran, W.M.; Fichtner, W.; Grosse, E.H.; Rose, D.J.; Smith, R.K. Transient simulation of silicon devise and circuits. *IEEE Trans. Comput.-Aided Des. Integr. Circuits Syst.* **1985**, *32*, 1992–2007.
5. Bathe, K.J.; Baig, M.M.I. On a composite implicit time integration procedure for nonlinear dynamics. *Comput. Struct.* **2005**, *83*, 2513–2524. [CrossRef]
6. Chandra, Y.; Zhou, Y.; Stanciulescu, I.; Eason, T.; Spottswood, S. A robust composite time integration scheme for snap-through problems. *Comput. Mech.* **2015**, *55*, 1041–1056. [CrossRef]
7. Wen, W.B.; Wei, K.; Lei, H.S.; Duan, S.Y.; Fang, D.N. A novel sub-step composite implicit time integration scheme for structural dynamics. *Comput. Struct.* **2017**, *182*, 176–186. [CrossRef]
8. Zhang, H.M.; Xing, Y.F. Optimization of a class of composite method for structural dynamics. *Comput. Struct.* **2018**, *202*, 60–73. [CrossRef]
9. Xing, Y.F.; Ji, Y.; Zhang, H.M. On the construction of a type of composite time integration methods. *Comput. Struct.* **2019**, *221*, 157–178. [CrossRef]
10. Noh, G.; Bathe, K.J. The Bathe time integration method with controllable spectral radius: The ρ_∞-Bathe method. *Comput. Struct.* **2019**, *212*, 299–310. [CrossRef]
11. Kim, W.; Choi, S.Y. An improved implicit time integration algorithm: The generalized composite time integration algorithm. *Comput. Struct.* **2018**, *196*, 341–354. [CrossRef]
12. Ji, Y.; Xing, Y.F. An optimized three-sub-step composite time integration method with controllable numerical dissipation. *Comput. Struct.* **2020**, *231*, 106210. [CrossRef]
13. Li, J.Z.; Yu, K.P.; Li, X.Y. A novel family of controllably dissipative composite integration algorithms for structural dynamic analysis. *Nonlinear Dyn.* **2019**, *96*, 2475–2507. [CrossRef]
14. Ji, Y.; Zhang, H.; Xing, Y.F. New insights into a three-sub-step composite method and its performance on multibody systems. *Mathematics* **2022**, *10*, 2375. [CrossRef]
15. Liu, T.H.; Huang, F.L.; Wen, W.B.; He, X.H.; Duan, S.Y.; Fang, D.N. Further insights of a composite implicit time integration scheme and its performance on linear seismic response analysis. *Eng. Struct.* **2021**, *241*, 112490. [CrossRef]
16. Zhang, J.Y.; Shi, L.; Liu, T.H.; Zhou, D.; Wen, W.B. Performance of a three-substep time integration method on structural nonlinear seismic analysis. *Math. Probl. Eng.* **2021**, *2021*, 6442260. [CrossRef]
17. Li, J.Z.; Zhao, R.; Yu, K.P.; Li, X.Y. Directly self-starting higher-order implicit integration algorithms with flexible dissipation control for structural dynamics. *Comput. Method Appl. Mech. Eng.* **2022**, *389*, 114274. [CrossRef]
18. Zhang, H.M.; Zhang, R.S.; Xing, Y.F.; Masarati, P. On the optimization of n-sub-step composite time integration methods. *Nonlinear Dyn.* **2021**, *21*, 2150073. [CrossRef]
19. Rezaiee-Pajand, M.; Sarafrazi, S.R. A mixed and multi-step higher-order implicit time integration family. *Proc. Inst. Mech. Eng. Part C J. Mech. Eng. Sci.* **2010**, *224*, 2097–2108. [CrossRef]
20. Kuhl, D.; Crisfield, M.A. Energy-conserving and decaying algorithms in non-linear structural dynamics. *Int. J. Numer. Methods Eng.* **1999**, *45*, 569–599. [CrossRef]
21. Park, K.C. Improved stiffly stable method for direct integration of nonlinear structural dynamics. *J. Appl. Mech. ASME* **1975**, *42*, 464–470. [CrossRef]
22. Belytschko, T.; Schoeberle, D.F. On the unconditional stability of an implicit algorithm for nonlinear structural dynamics. *J. Appl. Mech. ASME* **1975**, *42*, 865–869. [CrossRef]
23. Lavrencic, M.; Brank, B. Comparison of numerically dissipative schemes for structural dynamics: Generalized-alpha versus energy-decaying methods. *Thin-Wall. Struct.* **2020**, *157*, 107075. [CrossRef]
24. Xue, T.; Wang, Y.Z.; Aanjaneya, M.; Tamma, K.K.; Qin, G.L. On a generalized energy conservation/dissipation time finite element method for Hamiltonian mechanics. *Comput. Method Appl. Mech. Eng.* **2021**, *373*, 113509. [CrossRef]
25. Luo, J.H.; Feng, X.G.; Xu, X.M.; Peng, H.J.; Wu, Z.G. A parameter-preadjusted energy-conserving integration for rigid body dynamics in terms of convected base vectors. *Int. J. Numer. Methods Eng.* **2020**, *121*, 4921–4943. [CrossRef]
26. Zhang, H.M.; Xing, Y.F.; Ji, Y. An energy-conserving and decaying time integration method for general nonlinear dynamics. *Int. J. Numer. Methods Eng.* **2020**, *121*, 925–944. [CrossRef]

27. Chang, S.Y. Explicit pseudodynamic algorithm with unconditional stability. *J. Eng. Mech.* **2002**, *128*, 935–947. [CrossRef]
28. Chen, C.; Ricles, J.M. Development of direct integration algorithms for structural dynamics using discrete control theory. *J. Eng. Mech.* **2008**, *134*, 676–683. [CrossRef]
29. Kolay, C.; Ricles, J.M. Improved explicit integration algorithms for structural dynamic analysis with unconditional stability and controllable numerical dissipation. *J. Earthq. Eng.* **2019**, *23*, 771–792. [CrossRef]
30. Li, J.Z.; Yu, K.P.; Li, X.Y. A generalized structure-dependent semi-explicit method for structural dynamics. *J. Comput. Nonlinear Dyn.* **2018**, *13*, 111008. [CrossRef]
31. Namadchi, A.H.; Jandaghi, E.; Alamatian, J. A new model-dependent time integration scheme with effective numerical damping for dynamic analysis. *Eng. Comput.* **2021**, *37*, 2543–2558. [CrossRef]
32. Fu, B.; Zhang, F.T. A dual-explicit model-based integration algorithm with higher-order accuracy for structural dynamics. *Appl. Math. Model.* **2022**, *110*, 513–541. [CrossRef]
33. Soares, D. A simple and effective single-step time marching technique based on adaptive time integrators. *Int. J. Numer. Methods Eng.* **2017**, *109*, 1344–1368. [CrossRef]
34. Soares, D. Nonlinear dynamic analysis considering explicit and implicit time marching techniques with adaptive time integration parameters. *Acta Mech.* **2018**, *229*, 2097–2116. [CrossRef]
35. Soares, D. An improved adaptive formulation for explicit analyses of wave propagation models considering locally-defined self-adjustable time-integration parameters. *Comput. Method Appl. Mech. Eng.* **2022**, *399*, 115324. [CrossRef]
36. Soares, D. A locally stabilized explicit approach for coupled thermo-mechanical analysis. *Adv. Eng. Softw.* **2020**, *149*, 102883. [CrossRef]
37. Zhong, W.X.; Williams, F.W. A precise time step integration method. *Proc. Inst. Mech. Eng. Part C J. Mech. Eng. Sci.* **1994**, *208*, 427–430. [CrossRef]
38. Gao, Q.; Nie, C.B. An accurate and efficient Chebyshev expansion method for large-scale transient heat conduction problems. *Comput. Struct.* **2021**, *249*, 106513. [CrossRef]
39. Ding, Z.; Li, L.; Hu, Y.J. A modified precise integration method for transient dynamic analysis in structural systems with multiple damping models. *Mech. Syst. Signal Process.* **2018**, *98*, 613–633. [CrossRef]
40. Tian, W.; Yang, Z.C.; Gu, Y.S. Dynamic analysis of an aeroelastic airfoil with freeplay nonlinearity by precise integration method based on Padé approximation. *Nonlinear Dyn.* **2017**, *89*, 2173–2194. [CrossRef]
41. Ji, Y.; Xing, Y.F. Highly precise and efficient solution strategy for linear heat conduction and structural dynamics. *Int. J. Numer. Methods Eng.* **2022**, *123*, 366–395. [CrossRef]
42. Song, C.M.; Eisentrager, S.; Zhang, X.R. High-order implicit time integration scheme based on Padé expansions. *Comput. Method Appl. Mech. Eng.* **2022**, *390*, 114436. [CrossRef]
43. Li, L. A new symmetric linearly implicit exponential integrator preserving polynomial invariants or Lyapunov functions for conservative or dissipative systems. *J. Comput. Phys.* **2022**, *449*, 110800. [CrossRef]
44. Michels, D.L.; Luan, V.T.; Tokman, M. A stiffly accurate integrator for ealstodynamic problems. *ACM Trans. Graph.* **2017**, *36*, 116. [CrossRef]
45. Hammoud, B.; Olivieri, L.; Righetti, L.; Carpentier, J.; Prete, A. Exponential integration for efficient and accurate multibody simulation with stiff viscoelastic contacts. *Multibody Syst. Dyn.* **2022**, *54*, 443–460. [CrossRef]
46. Chen, Y.J.; Ascher, U.M.; Pai, D.K. Exponential rosenbrock-euler integrators for elastodynamic simulation. *IEEE Trans. Vis. Comput. Graph.* **2018**, *24*, 2702. [CrossRef]
47. Hochbruck, M.; Ostermann, A. Exponential integrators. *Acta Numer.* **2010**, *19*, 209–286. [CrossRef]
48. Fung, T.C. Construction of higher-order accurate time-step integration algorithms by equal-order polynomial projection. *J. Vib. Control* **2005**, *11*, 19–49. [CrossRef]
49. Nettesheim, P.; Bornemann, F.A.; Schmidt, B.; Schutte, C. An explicit and symplectic integrator for quantum-classical molecular dynamics. *Chem. Phys. Lett.* **1996**, *256*, 581–588. [CrossRef]
50. Rambeerich, N.; Tangman, D.Y.; Gopaul, A.; Bhuruth, M. Exponential time integration for fast finite element solutions of some financial engineering problems. *J. Comput. Appl. Math.* **2009**, *224*, 668–678. [CrossRef]
51. Matute, J.; Pardo, D.; Demkowicz, L. Equivalence between the DPG method and the exponential integrators for linear parabolic problems. *J. Comput. Phys.* **2021**, *429*, 110016. [CrossRef]
52. Zhang, J.; Liu, Y.L.; Liu, D.H. Accuracy of a composite implicit time integration scheme for structural dynamics. *Int. J. Numer. Methods Eng.* **2017**, *109*, 368–406. [CrossRef]
53. Maxam, D.J.; Tamma, K.K. A re-evaluation of overshooting in time integration schemes: The neglected effect of physical damping in the starting procedure. *Int. J. Numer. Methods Eng.* **2022**, *123*, 2683–2704. [CrossRef]
54. Chang, S.Y. A novel series of solution methods for solving nonlinear stiff dynamic problems. *Nonlinear Dyn.* **2022**, *107*, 2539–2562. [CrossRef]
55. Rezaiee-Pajand, M.; Alamatian, J. Implicit higher-order accuracy method for numerical integration in dynamic analysis. *J. Struct. Eng.* **2008**, *134*, 973–985. [CrossRef]
56. Loh, C.H.; Mao, C.H.; Huang, J.R.; Pan, T.C. System identification and damage evaluation of degrading hysteresis of reinforced concrete frames. *Earthq. Eng. Struct. Dyn.* **2011**, *40*, 623–640. [CrossRef]
57. Yang, Y.; Ma, F. Constrained Kalman filter for nonlinear structural identification. *J. Vib. Control* **2003**, *9*, 1343–1357. [CrossRef]

58. Sengupta, P.; Li, B. Modified Bouc-Wen model for hysteresis behavior of RC beam -column joints with limited transverse reinforcement. *Eng. Struct.* **2013**, *46*, 392–406. [CrossRef]
59. Ji, Y.; Xing, Y.F.; Wiercigroch, M. An unconditionally stable time integration method with controllable dissipation for second-order nonlinear dynamics. *Nonlinear Dyn.* **2021**, *105*, 3341–3358. [CrossRef]
60. Zhang, H.M.; Zhang, R.S.; Masarati, P. Improved second-order unconditionally stable schemes of linear multi-step and equivalent single-step integration methods. *Comput. Mech.* **2021**, *67*, 289–313. [CrossRef]